

Diagnosis of mixing between middle latitudes and the polar vortex from tracer-tracer correlations

Olaf Morgenstern¹ and John A. Pyle

Centre for Atmospheric Science, Chemistry Department, Cambridge University, Cambridge, UK

Alan M. Iwi and Warwick A. Norton

Atmospheric, Oceanic and Planetary Physics, Department of Physics, Oxford University, Oxford, UK

James W. Elkins, Dale F. Hurst, and Pavel A. Romashkin

NOAA Climate Monitoring and Diagnostics Laboratory, Boulder, Colorado, USA

Received 16 August 2001; revised 18 December 2001; accepted 8 January 2002; published 5 September 2002.

[1] A method is introduced for diagnosing mixing between the polar vortex and midlatitudes from tracer data. Tracers with different photochemical activities and lifetimes usually exhibit curved tracer-tracer correlation functions on an isentropic surface. The effect of mixing events is to populate the inner side of such a curve. Using simultaneous measurements of trace gases or model results, we exploit this process to calculate the distribution of recent origins in tracer space prior to such a mixing event. The method relies on both hemispheric and local data and is applicable to situations where mixing is nonlocal in tracer space. It is applied to measurements taken during the Stratospheric Aerosol and Gas Experiment (SAGE) III Ozone Loss and Validation Experiment/Third European Stratospheric Experiment on Ozone 2000 (SOLVE/THESEO 2000) winter campaign and to a chemical transport model simulation covering the same winter. In one of the cases studied, a vortex breakup and subsequent reemergence of the vortex fragments in March 2000 results in significant diagnosed mixing. In a further example, an elongated filament shed off the polar vortex is characterized by anomalous composition. For the two high-altitude aircraft flights of the SOLVE campaign that probe the vortex boundary, a correspondence is found for mixing diagnosed in the measurements and in the model. Mixing timescales considered here are given by the life span of planetary waves, up to a few weeks.

INDEX TERMS: 0341 Atmospheric Composition and Structure: Middle atmosphere—constituent transport and chemistry (3334); 3319 Meteorology and Atmospheric Dynamics: General circulation; 3337 Meteorology and Atmospheric Dynamics: Numerical modeling and data assimilation;

KEYWORDS: stratosphere, tracer, mixing, polar vortex, midlatitudes, canonical correlation

Citation: Morgenstern, O., J. A. Pyle, A. M. Iwi, W. A. Norton, J. W. Elkins, D. F. Hurst, and P. A. Romashkin, Diagnosis of mixing between middle latitudes and the polar vortex from tracer-tracer correlations, *J. Geophys. Res.*, 107(D17), 4321, doi:10.1029/2001JD001224, 2002.

1. Introduction

[2] Tracer-tracer correlations are often invoked to assess transport and mixing in the stratosphere. Pairs of long-lived tracers generally form compact correlations (e.g., *Goldan et al.* [1980], as referenced by *Plumb* [1996], *Kelly et al.* [1989], and *Fahey et al.* [1990]). Different regions of the atmosphere are characterized by different such tracer relationships, e.g., the tropics and the midlatitudes [*Volk et al.*, 1996]. A similar partitioning into different regimes emerges in an analysis of probability density functions of tracer mixing ratios [*Sparling*, 2000].

[3] An example of a tracer-tracer correlation plot is displayed in Figure 1. In this model result the parameter space displayed in Figure 1 spanned by the two tracers is populated to a very variable density. Like in the observations, polar-vortex, midlatitude, and tropical “canonical correlations” show up as ridges in the density plot, marked as “P”, “ML”, and “T”, respectively. *Plumb and Ko* [1992] discuss these correlations. They reflect the different compositions, ages, and photochemical histories of air parcels in those three regions of the atmosphere [*Schoeberl et al.*, 2000]. In the following, the (multidimensional) tracer parameter space is referred to as “tracer space”.

[4] The formation of different tracer-tracer correlations in different atmospheric reservoirs is a consequence of the presence of transport barriers [*Haynes and Shuckburgh*, 2000, Figure 1]. The robustness of these correlations has

¹Now at Max-Planck-Institut für Meteorologie, Hamburg, Germany.

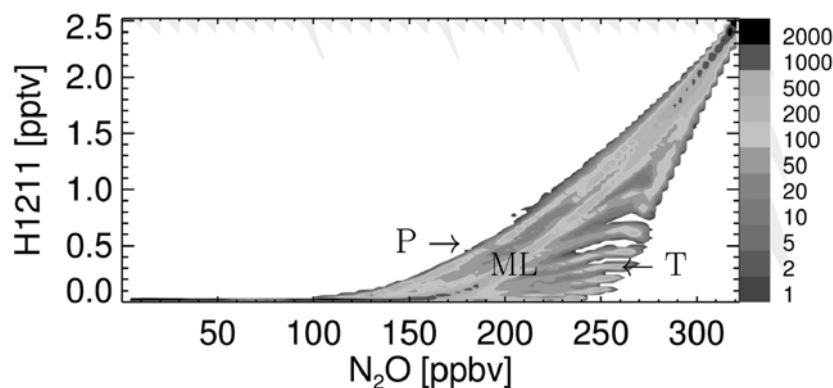


Figure 1. Density plot of halon-1211 versus N_2O for the SLIMCAT integration at 9 March 2000. The model data of the Northern Hemisphere above 342 K of potential temperature are binned into 100×100 intervals of mixing ratio; displayed is the number of grid points per bin. The model comprises 640,000 grid points in the Northern Hemisphere. See color version of this figure at back of this issue.

been used to quantify ozone depletion [e.g., Proffitt *et al.*, 1989], dehydration [Kelly *et al.*, 1989], and denitrification [Fahey *et al.*, 1990], provided however mixing processes can be discriminated against chemistry [Rex *et al.*, 1999; Plumb *et al.*, 2000; Salawitch *et al.*, 2002]. Explicitly calculating the local budgets of trace species, Minschwaner *et al.* [1996] and Volk *et al.* [1996] use the difference of tracer-tracer relationships between the tropics and the midlatitudes to give estimates of mixing timescales between the two reservoirs. An application of their method to the polar vortex would require a modification because of the greater importance of the seasonal cycle in high latitudes, compared to the tropics.

[5] Anomalous mixing has been observed in tracer data [e.g., Waugh *et al.*, 1997; Michelsen *et al.*, 1998]. In the wake of, for example, a major wave breaking event air parcels from different reservoirs are brought together and mixed, creating, by way of a linear superposition of their trace gas mixing ratios, a straight line across an otherwise thinly populated part of tracer space. However, such mixing lines are constrained by the approximately isentropic nature of transport and mixing, so mixing lines can only connect points on the canonical correlations that represent approximately the same isentropic level. Thus mixing is not only inhibited by the presence of transport barriers (such as the boundary of the polar vortex) but also by separations in potential temperature. Hence different “isentropic correlation functions” relating pairs of tracers may be expected to develop on different isentropic surfaces, reflecting the different average photochemical histories of air parcels on these surfaces [Schoeberl *et al.*, 2000, Plate 1]. An example is displayed in Figure 1, where in a part of tracer space a separation of the data points according to the isentropic levels of the underlying chemical transport model may be discerned (i.e., the “fingers” in the bottom right corner of Figure 1 corresponding to different isentropic model surfaces). Thus, alternatively to having tracer-tracer correlations depend on equivalent latitude (which effectively is the conventional approach), the set of correlative tracer data can be described equally by correlation functions parameterized with potential temperature. On the two hemispheres, tracers may develop different isentropic and canonical correlations, so here all further analysis is restricted to one hemisphere only.

[6] A contribution to mixing is brought about by nonuniform diabatic heating, leading to cross-isentropic dispersion of air parcels. Sparling *et al.* [1997] show that this dispersion is much smaller inside the polar vortex than in midlatitudes, suggesting that the polar vortex sees a relatively uniform subsidence with little interlevel mixing. Clearly, however, diabatic dispersion is a mechanism broadening correlative tracer sets, in competition with isentropic mixing. The topic is further discussed in section 7.

[7] If both chemistry and diabatic motion are slow compared to the adiabatic component of advection, then linear relationships ensue between pairs of such long-lived tracers [Plumb and Ko, 1992]. Timescales of mixing within atmospheric regions separated by transport barriers often satisfy this condition but timescales describing mixing between different regions may not. In such a situation one finds curved isentropic correlations (e.g., Figure 2). If in a thought experiment one takes two parcels from the same isentropic surface with mixing ratios of the two tracers matching the curved correlation and generates a linear superposition of their tracer mixing ratios (i.e., a mixture), the result is an air mass with anomalous tracer concentrations lying off the isentropic correlation curve, as in the studies cited above.

[8] The present paper will exploit this relationship between mixing and the distance of a tracer data pair from the corresponding “isentropic” correlation curve. It will introduce a methodology through which the process of the formation of mixing lines may be inverted to yield information about the distribution of recent positions of parcels in tracer space immediately prior to the mixing event that make up the observed or modeled mixed parcel. The timescales considered are hence those for isentropic stirring in the wake of planetary waves. The method depends on both local and hemispheric information, i.e., the local mixing ratios of a number of tracers at a point in time and space and their respective isentropic correlations.

[9] The method will be applied to the lower stratosphere during the 1999/2000 Arctic winter and spring. This period saw the comprehensive international measurement campaign Stratospheric Aerosol and Gas Experiment (SAGE) III Ozone Loss and Validation Experiment/Third European Stratospheric Experiment on Ozone 2000 (SOLVE/THESEO 2000), yielding a substantial amount of stratospheric tracer

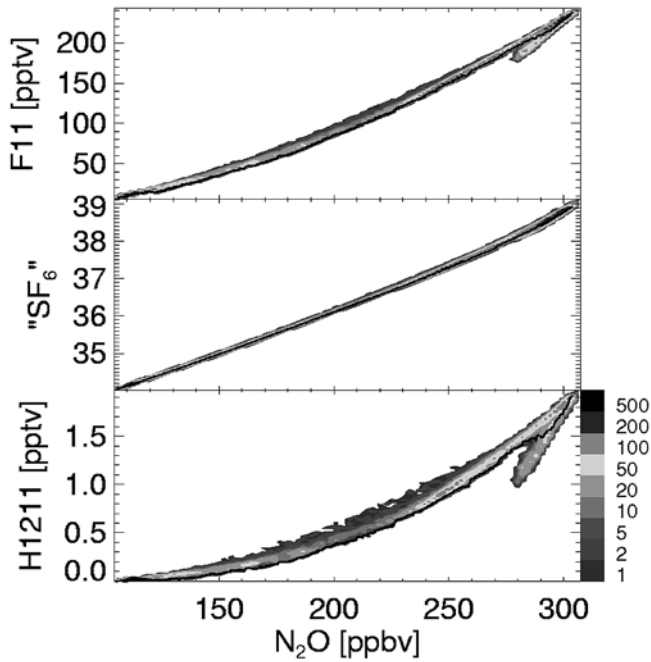


Figure 2. Density scatter plot of CFC-11, SF_6 (arbitrary units), and halon-1211 versus N_2O , for the 451 K isentropic surface at 1 March 2000, 1200 UTC, taken from the SLIMCAT integration. The black lines mark the correlation envelopes $\Psi_i(\zeta; \Theta, t)$. See color version of this figure at back of this issue.

measurements. In the following, we will develop the methodology and show its application both to model results and to SOLVE measurements.

2. The Method

[10] Figure 2 depicts density plots of pairs of long-lived species taken from a model simulation, sampled on the 451 K isentropic model surface. The data form compact correlations with the most long-lived tracer computed by the model, N_2O . Two maxima of data density are evident in the Figure 2, defining the most typical mixing ratios in the polar vortex (about 115 ppbv of N_2O , labeled “P”) and in midlatitudes (about 250 ppbv of N_2O , labeled “ML”) at this isentropic level. For halon-1211 and CFC-11 the isentropic correlations with N_2O are positively curved. Here we adopt the viewpoint that data points on the inner sides of these curves result from mixing between high and middle latitudes; this will be formalized in the following. In the tropics (the top right corners of the plots) separate branches appear, constituting parts of the tropical canonical correlations. In computing the displayed isentropic correlation envelopes these branches are suppressed by excluding points south of 35° from the computation of the isentropic correlation envelopes (Figure 2). Accordingly, here the focus is on exchange between midlatitudes and the polar vortex only. The inner and outer sides of the isentropic correlation curves are marked “A” and “B”. In defining inner and outer sides the assumption is made that the sign of curvature does not change outside of the tropics; this is further elaborated in section 7.

[11] To formalize the above, let $\Psi(\zeta; \Theta, t) = (\Psi_1, \dots, \Psi_p)$ be the set of “correlation envelopes” bounding a set of corre-

lative tracer data on the outer (B) side (see Appendix B for details). Here, ζ denotes the reference tracer N_2O , Θ is potential temperature, and the analysis time t accounts for a possible slow evolution with season. N_2O is chosen as the reference tracer because it has a good contrast across both the edge of the polar vortex and the subtropical barrier. There are p different tracers considered here. By definition the reference tracer satisfies $\Psi_1(\zeta) = \zeta$. Examples are displayed in Figures 2 and 3a. The Ψ_i describe an idealized, “unmixed” atmosphere where correlative data points of pairs of long-lived tracers form compact curves on an isentropic surface. The two lines depicted in Figure 3a illustrate two possibilities for isentropic mixing of points on a correlation envelope which can generate, by way of a weighted linear combination, any point on the mixing lines. For the measurement depicted, both lines are possible, as is indeed a range of intermediate possibilities. In a generalization of the mixing of exactly two points on the correlation envelope to form a mixing line, a range of origins may be responsible for generating the observed air mass (as postulated by *Plumb et al.* [2000]). In the example considered, the weighting function (“mixing kernel”) $h(\zeta)$ shown in Figure 3b characterizes such a situation whereby air from a range of low mixing ratios of ζ mixes with air from a range of high ζ . Hence $h(\zeta) d\zeta$ describes the relative fraction of an air mass originating in the infinitesimal region of reference tracer mixing ratio $[\zeta, \zeta + d\zeta]$, so h constitutes a quantification of the air parcel’s composition and hence mixing. Formally, h satisfies

$$\psi_i(\mathbf{x}, t) = \int h(\zeta; \mathbf{x}, t) \Psi_i(\zeta; \Theta, t) d\zeta, \quad (1)$$

with $\psi(\mathbf{x}, t) = (\psi_1, \dots, \psi_p)$ denoting the set of p different tracers modeled or observed at a given point of time and

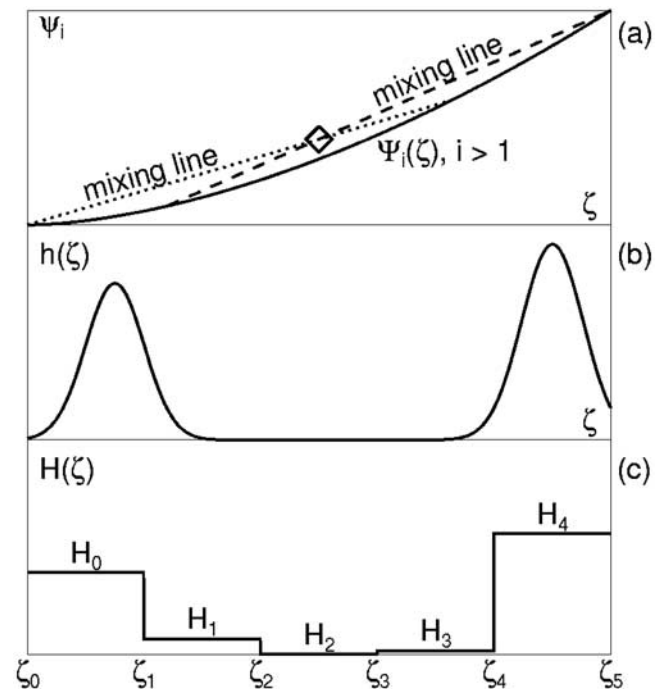


Figure 3. Illustration of method. (a) Solid line: Isentropic correlation $\Psi_i(\zeta)$. Diamond: measurement. (b) Mixing kernel $h(\zeta)$. (c) Approximate mixing kernel $H(\zeta)$, a step function.

space, with $\mathbf{x} = (\lambda, \phi, \Theta)$ comprising the spatial coordinates longitude λ , latitude ϕ , and Θ . (In particular, Ψ describes the composition of the atmosphere at the isentropic level containing \mathbf{x} .) Equation (1) expresses mathematically the notion that the composition of the atmosphere at (\mathbf{x}, t) is the result of a linear mixing of points originating on the isentropic correlation envelopes. Correspondingly, the integral in equation (1) extends over the range of values which ζ attains on the isentropic surface of the measurement, restricted to one hemisphere. As a weighting function h is normalized and nonnegative, i.e., $\int h(\zeta; \mathbf{x}, t) d\zeta = 1$ and $h \geq 0$. All tracers experience the same mixing. Hence if h is reconstructed from a set of tracers (as will be done in the following), the exact choice of tracers may be of little relevance. For simplicity, the additional dependencies of h , ψ_i , and Ψ_i on the spatial and temporal coordinates \mathbf{x} , Θ , and t will be understood in the following.

[12] Under the assumption that equation (1) holds exactly in the real stratosphere for p different tracers, the mixing kernel h can be determined approximately. Let $H(\zeta; \mathbf{x}, t) \approx h(\zeta; \mathbf{x}, t)$ be an approximate solution to equation (1); H is taken to be a piecewise constant (i.e., a step-) function in ζ . It is hence denoted as $H(\zeta; \mathbf{x}, t) = \sum_k H_k(\mathbf{x}, t) s_k(\zeta; \Theta, t)$, where the s_k denote the rectangular functions describing the k th bin. The approximate mixing kernel H then does not exactly satisfy equation (1); instead, at every model grid point or for every measurement $H(\zeta)$ minimizes the quadratic form

$$f(H; \mathbf{x}, t) = \left\| \psi(\mathbf{x}, t) - \int H(\zeta; \mathbf{x}, t) \Psi(\zeta) d\zeta \right\|^2 \quad (2)$$

under the conditions $\int H(\zeta) d\zeta = 1$ and $H(\zeta) \geq 0$. An example is displayed in Figure 3c. Details about the particular choice of the norm $\| \cdot \|$ in equation (2) measuring distances in p -dimensional tracer space, and how H is determined, are given in Appendix A. The computation of the correlation envelopes Ψ_i is explained in Appendix B. The result, in the cases considered here, may be expressed as a 5-dimensional vector field $\mathbf{h}(\mathbf{x}, t) = (H_0, \dots, H_4)$ representing the step function $H(\zeta; \mathbf{x}, t)$ which describe the contribution to the composition from any of five atmospheric regions. This choice of dimensionality means that with four atmospheric tracers available in the model simulation (described in section 3) and the normalization constraint the minimization problem is mathematically well posed. The vector field \mathbf{h} is normalized such that $\sum H_k = 1$; the components H_k describe the fraction of air found at a given grid point originating from the k th interval (“bin”) $[\zeta_k, \zeta_{k+1}]$ of mixing ratios of the reference tracer ζ . Components of \mathbf{h} will be displayed as isentropic maps.

[13] In Figure 3, if low mixing ratios of ζ denote core-vortex air and high mixing ratios subtropical air (as in Figure 2), then the considered air mass (the diamond in Figure 3a) has contributions both from the polar vortex and from the subtropics, indicating that it is of a mixed nature. In general, if the product of two bin amplitudes, $H_k \cdot H_l$, does not vanish, this indicates contributions from both bins and hence mixing. However, note that due to the nature of the approximation, for an air parcel with ζ close to a bin boundary ζ_k the method will usually generate nonzero amplitudes of both H_{k-1} and H_k without the parcel having

to be of a mixed nature. Hence in the above it will only be of interest to analyze the products of nonneighboring bins with $|k - l| \geq 2$, i.e., for long-range mixing in tracer space. The normalization implies that $H_k \cdot H_l \leq 1/4$. If the product equals 1/4, it means the product is composed of 50% contributions each from both bins.

[14] By its nature the above formalism does not account for diabatic motion. Hence in the formulation given here it cannot be used to infer long-term, “cumulative” effects of mixing, whereby mixing and diabatic motion change isentropic tracer-tracer correlation functions on similar time-scales. In the following, we assess the method’s capability of identifying regions of “instantaneous” mixing characterized by a relatively large distance between the vector of measured mixing ratios and their corresponding isentropic correlation function. A related, more general formalism that will allow to assess cumulative mixing is postponed to a future publication.

[15] In the following sections the method is applied to model and measurement data.

3. The SLIMCAT Model

[16] The version of the chemical transport model SLIMCAT used here is a high-resolution variant of the one described by *Chipperfield* [1999]. It covers the region of potential temperature between 335 K and 3000 K with 25 isentropic levels at a resolution of T106, corresponding to a grid spacing of about 1.1°. Horizontal winds, temperature and pressure are taken from European Centre for Medium-Range Weather Forecasts (ECMWF) analyses. Vertical winds are computed using the MIDRAD middle atmosphere radiation scheme [*Shine*, 1987], employing a climatological zonally symmetric ozone field to calculate radiative forcing. Transport is computed using the *Prather* [1986] advection scheme. The diagnosis of mixing relies on modeled fields of N₂O, CCl₃F (CFC-11), an SF₆-like tracer with a bottom boundary condition increasing linearly with time, and CF₂BrCl (halon-1211). N₂O, CFC-11, and halon-1211 photochemistries depend on solar zenith angle and pressure, while SF₆ is completely inert. The model is initialized on 10 October 1999, from a 15-months spinup simulation at T42. The high-resolution integration uses ECMWF analyses at T106/L60. Examples of model-produced tracer-tracer correlations are shown in Figures 1 and 2. The same model simulation is used and described by *Piani et al.* [2002].

4. Meteorology of the Winter of 1999/2000

[17] In contrast to the preceding two winters, the winter of 1999/2000 was characterized by low temperatures and extensive formation of polar stratospheric clouds (PSCs), starting in late November 1999 and lasting until early March 2000 [*Sinnhuber et al.*, 2000]. At around the turn of the year, the vortex reached its mature stage. A comparatively quiet period ensues in January 2000 with some filamentation visible in the simulations (section 3) in the region of the ozone layer (~450 K). In mid-February the stability started to decrease, with some wave amplification leading eventually to an asymmetric splitting of the vortex at 18 February. During the subsequent days, the smaller of the two fragments was wrapped around the larger. This case will be

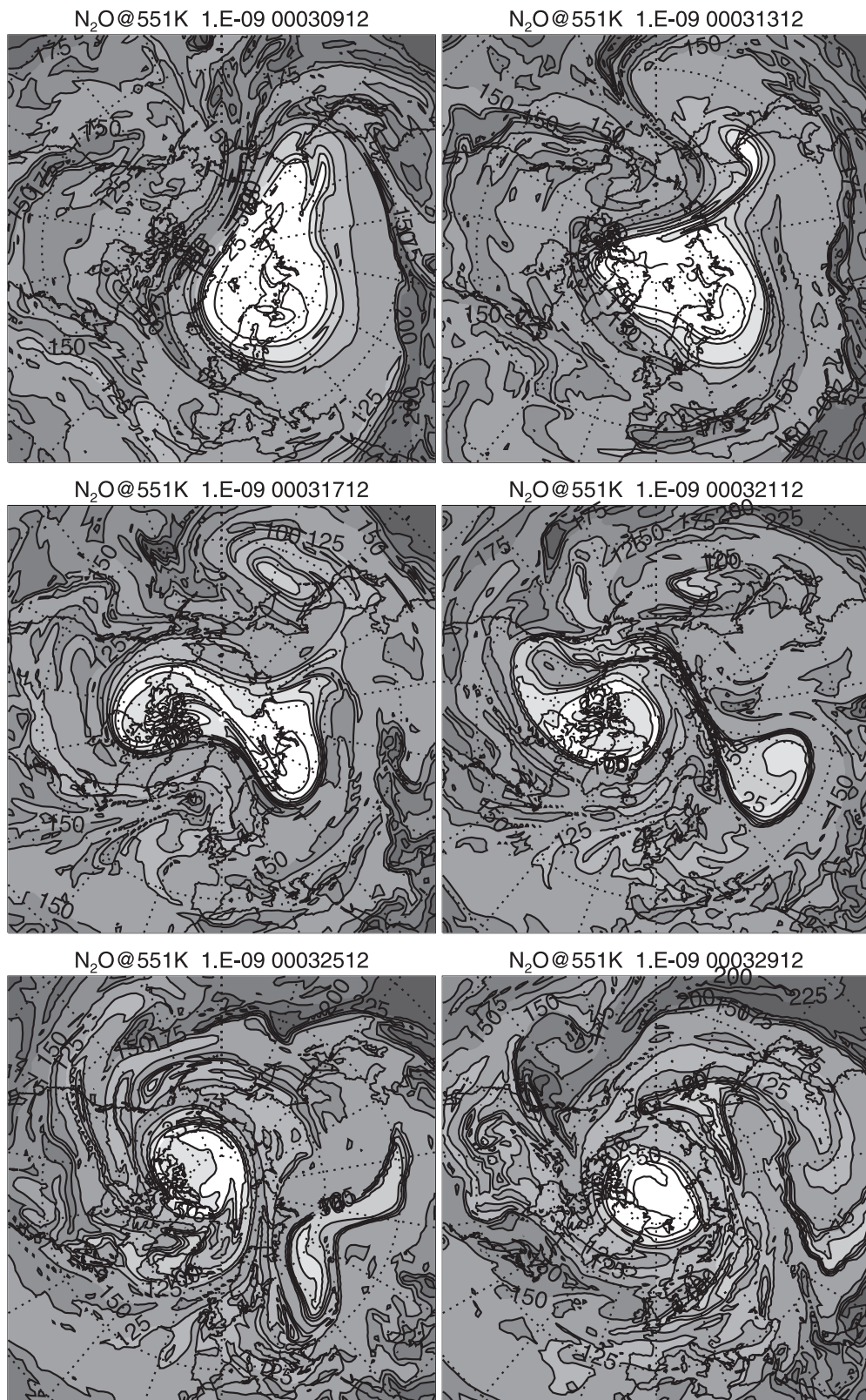


Figure 4. N₂O mixing ratio in ppbv at 551 K from 9 to 29 March 2000, 1200 UTC each, at 4-day intervals, from the SLIMCAT integration.

Table 1. Positions of Bin Boundaries ζ_k^a

k	0	1	2	3	4	5
ϕ_e	90°	80°	70°	60°	40°	0°
ζ_k (case A)	16	23	51	121	145	268
ζ_k (case B)	110	115	133	201	262	308

^aReferring to the different bins of the weighting kernel H given in terms of the N_2O equivalent latitude Φ_e and the corresponding N_2O mixing ratios in ppbv for case A, 9 March 2000, 1200 UTC, 551 K and case B, for 18 February 2000, 1200 UTC, 451 K.

analyzed in some detail. March then saw a significant increase in wave activity; the vortex again broke into several pieces. This final stage of a continuous vortex will also be analyzed.

5. Results of Model Simulations

5.1. Case Study: Breakup and Remerging of the Polar Vortex

[18] Figure 4 displays the evolution of the polar vortex at the 551 K isentropic surface in March 2000, as simulated by

SLIMCAT. The N_2O mixing ratio, chosen to visualize the vortex structure, shows much the same pattern as the other long-lived tracers. On 9 March the vortex was largely unperturbed, though elongated, with a clearly defined edge. During the subsequent three weeks a planetary wave amplified, led to a vortex breakup, and then the fragments remerged to form a highly structured new vortex.

[19] For every time the mixing analysis is presented here, the correlation functions Ψ_i are computed and the approximate mixing correlation kernel $H(\zeta; \mathbf{x}, t)$ is determined at the 551 K isentropic level (see section 2 and appendices for the method). The 6 bin boundaries which define H (Figure 3c) are given in Table 1 in terms of their equivalent N_2O -latitude. For 9 March 2000 they correspond to the stated mixing ratios ζ_k which change slowly during the course of the integration.

[20] The bins H_0 and H_1 (corresponding to 80–90° and 70–80° in equivalent latitude) mark the polar vortex, H_2 its outer boundary, H_3 midlatitudes, and H_4 low-latitude air (Figure 5). The temporal evolution of H_0 is displayed in Figure 6. For early March 2000 H_0 takes nonzero values in

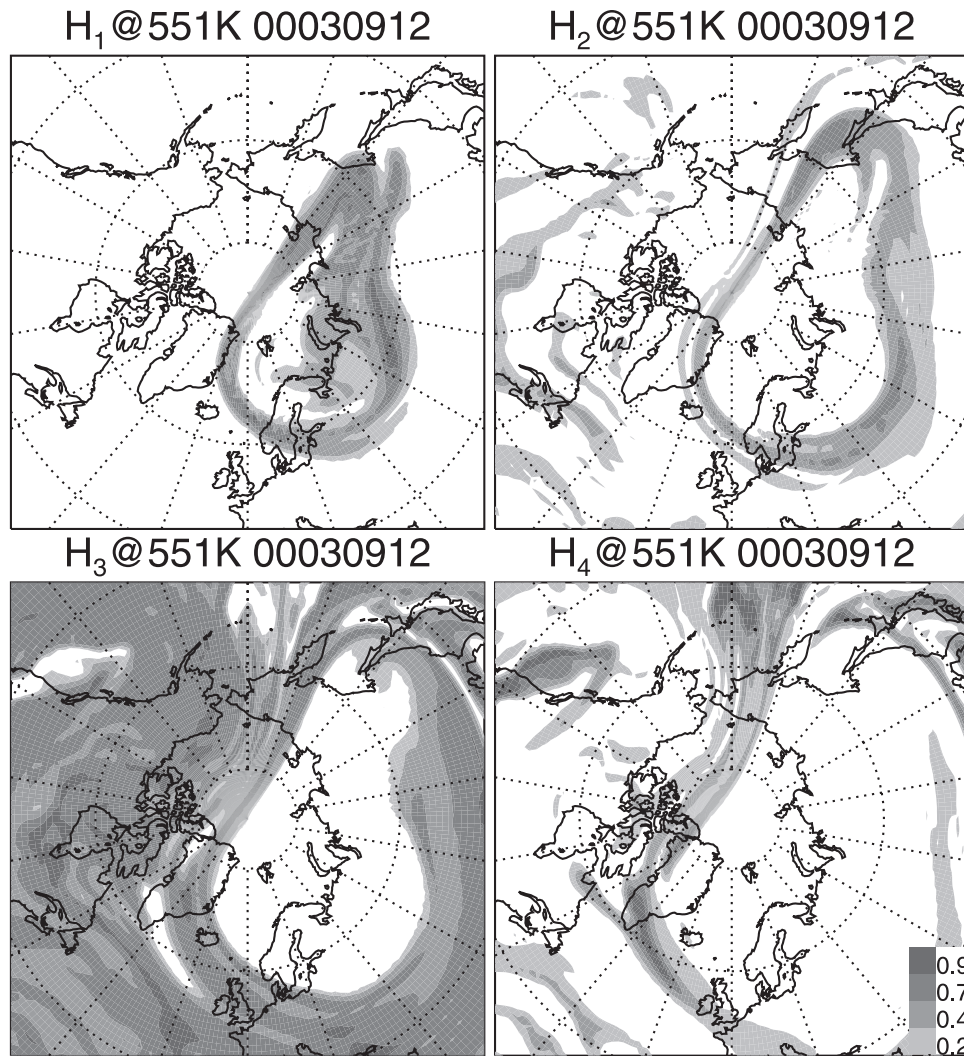


Figure 5. Amplitudes H_k of associated with the different latitude bins, at 9 March 2000, 1200 UTC, on the 551 K isentropic surface. Displayed are the bins 1 (inner boundary of the polar vortex), 2 (outer boundary of the polar vortex), 3 (midlatitude air), and 4 (subtropical air).

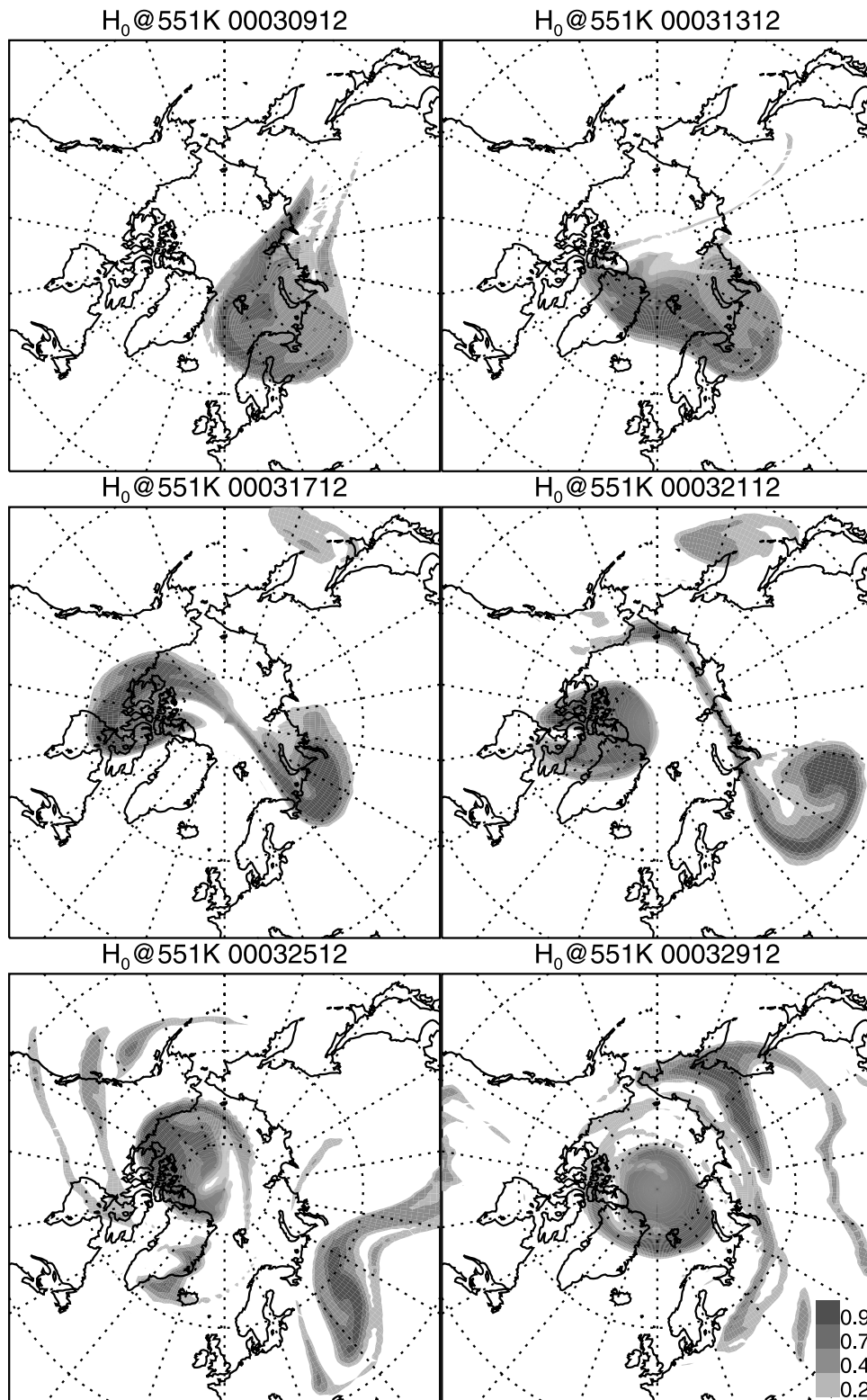
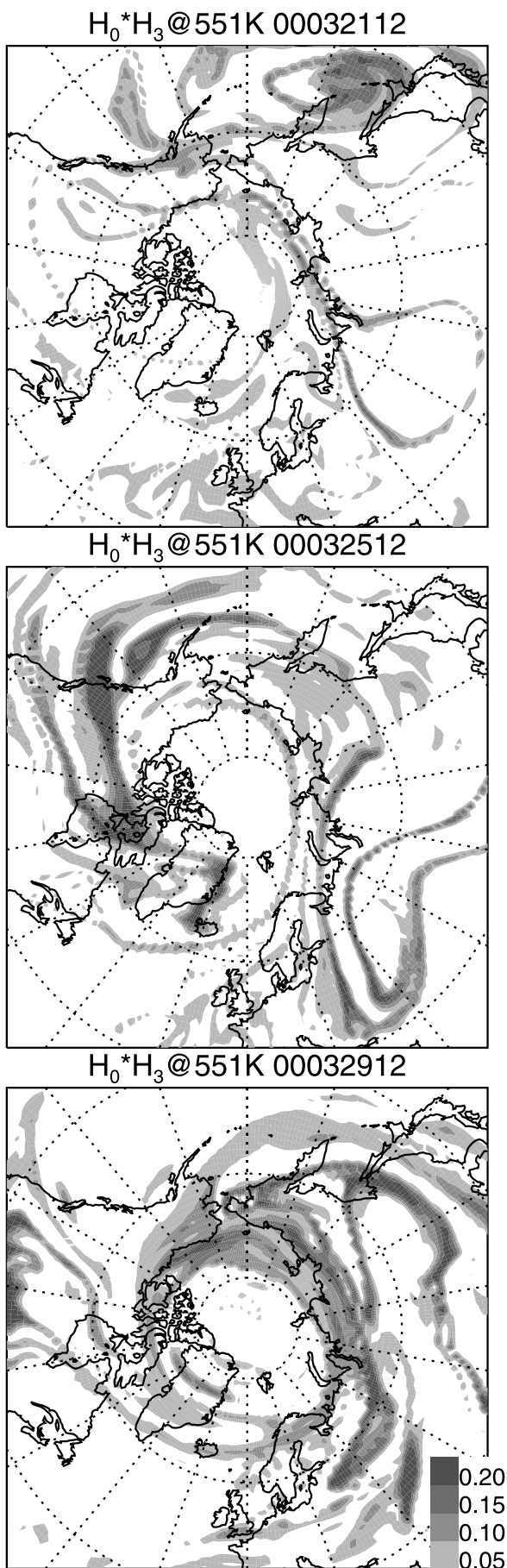


Figure 6. Same as Figure 5, but for H_0 (core of the polar vortex) from 9 to 29 March 2000, 1200 UTC, at 4-day intervals.

the core of the polar vortex. At 17 March a vortex fragment appears over the western Pacific. During the break-up and remerging of the vortex from 17 to 29 March some filamentary structure appears. To visualize regions of mixed air we compute products of nonneighbor-

ing bins (there are 6 such pairs). The pair (H_0, H_3) has the strongest overlap of all combinations of bins in the later stages of the event (Figure 7), and the pattern of the overlap singles out filamentary structure evident in Figures 4 and 6. Thus for this event the method mainly



diagnoses mixing of air from the vortex core ($80\text{--}90^\circ$) with middle latitude air.

5.2. Case Study: Filamentation of the Polar Vortex

[21] The example detailed in section 5.1 constituted a rather large event associated with the final decay of the vortex. More commonly, especially during midwinter, filaments are shed off the otherwise largely undisturbed vortex. An example is displayed in Figure 8, showing the bin amplitude H_2 as diagnosed from the SLIMCAT simulation. (For the corresponding positions of the bin boundaries, see Table 1). As before, H_2 marks the edge of the vortex. The previously mentioned asymmetric splitting, starting in mid-February, eventually leads to the formation of an elongated filament encircling most of the Northern Hemisphere (including Asia, the Mediterranean, the Atlantic Ocean, and North America) on 1 March 2000. The only non-neighboring pair of bin amplitudes H_k exhibiting any significant overlap is (H_2, H_4) whose product is displayed in Figure 9. The picture indicates that air originating in the vortex boundary has mixed with subtropical air.

5.3. Summary of Model Experiments

[22] The method has been applied to two examples of mixing in the wake of major wave breaking events. In both cases, the anomalous composition of filaments formed in these episodes is exploited to approximately reconstruct the distribution of recent origins prior to the mixing events. We now apply the method to measurements.

6. Application of Method to Measurements

6.1. ER-2 Measurements Taken During the SOLVE/ THESEO Campaign

[23] Further analysis here will focus on trace gas measurements taken on board the ER-2 aircraft during its participation in SOLVE/THESEO 2000 on flights out of Kiruna, Sweden (68°N , 20°E), from 6 January to 18 March 2000, with a break from 3 to 26 February. Also measurements made during December 1999 on flights out of Dryden, California (35°N , 118°W), and during transit flights are taken into account for the determination of general data properties. The flights of 27 January and 11 March are the only ones which probed the boundary of the polar vortex; they will be analyzed in detail. Meteorological data and long-lived trace gas data measured by the ACATS IV gas chromatograph [Elkins *et al.*, 1996] are used for the following analysis.

6.2. Instruments and Observational Data

[24] The ACATS instrument yields measurements of up to 11 long-lived species. Table 2 summarizes some global data properties.

[25] The “mean” relative uncertainty for a given species is defined as the median of the ratios e_j/c_j , where c_j and e_j denote the measured mixing ratios and their respective absolute uncertainties. In the determination of mean relative measurement uncertainties care needs to be taken with measurements with near-zero mixing ratios which could

Figure 7. (opposite) Same as Figure 6, but for $H_0 \cdot H_3$ for 21, 25, and 29 March 2000, 1200 UTC.

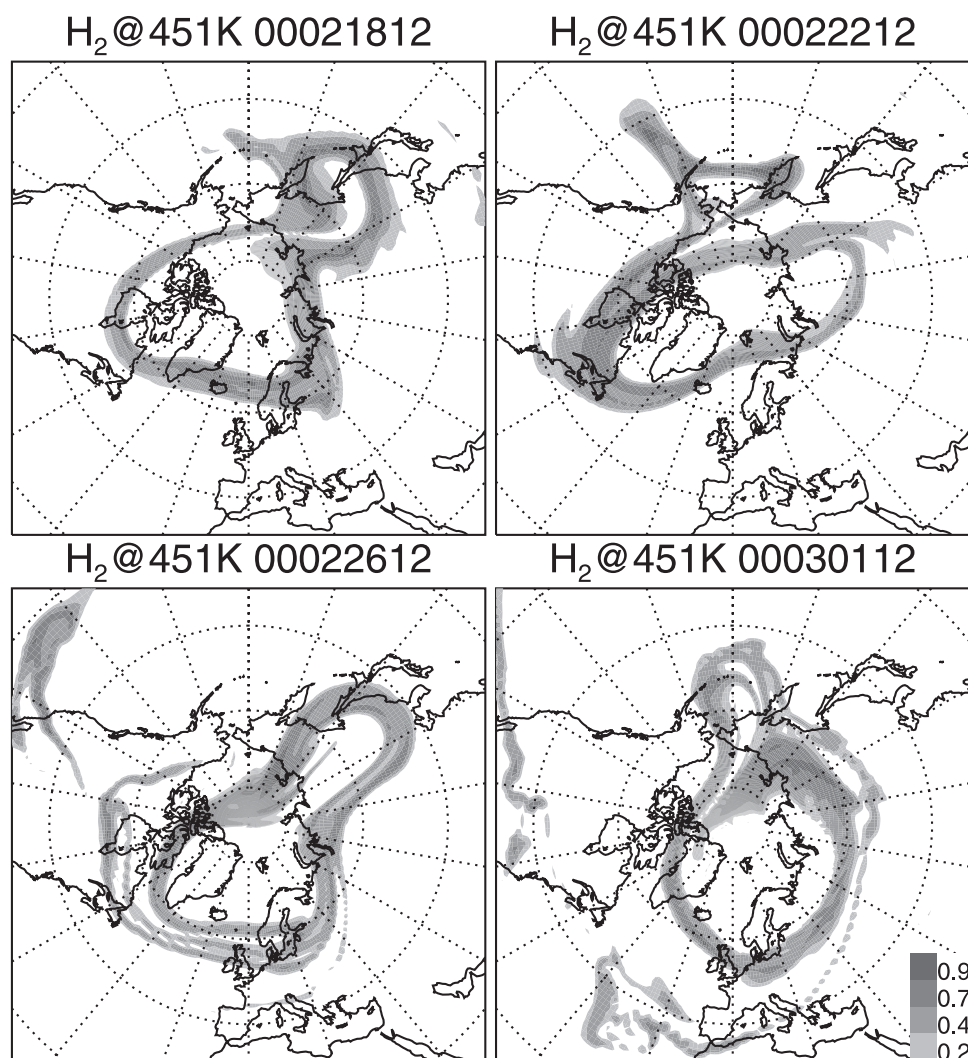


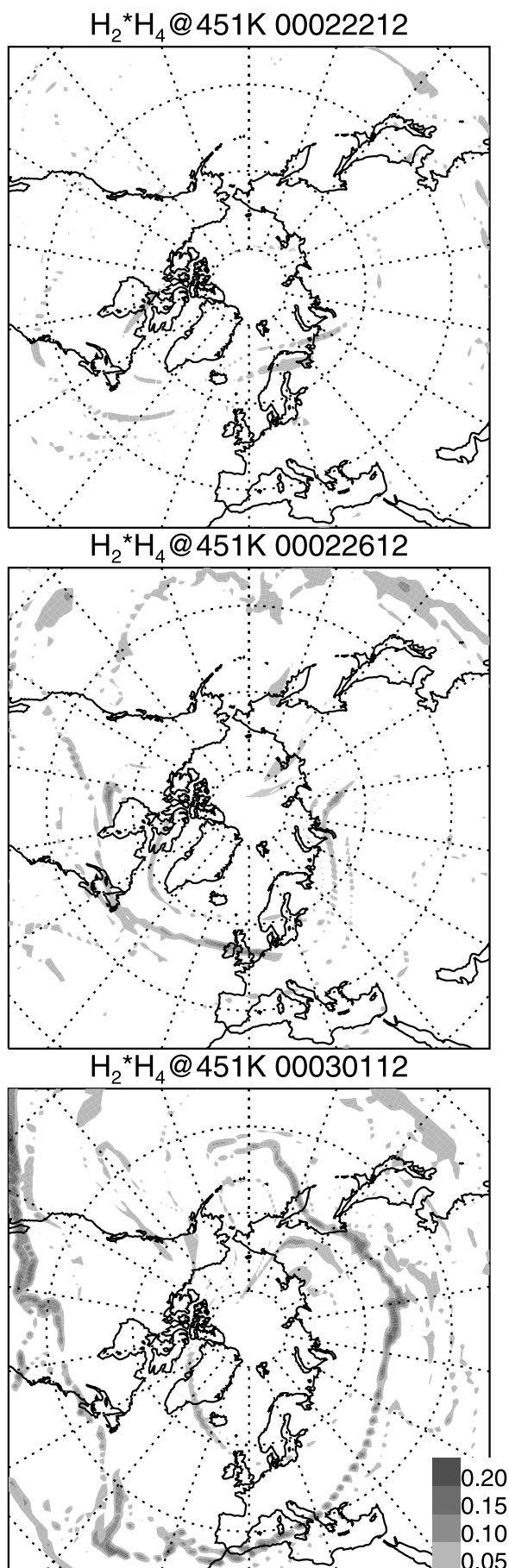
Figure 8. Mixing kernel amplitude H_2 at 451 K from 18 February to 1 March 2000, at 4-day intervals from the SLIMCAT integration.

dominate the results. Hence in Table 2b only measurements with mixing ratios exceeding twice their absolute uncertainties are considered. The comparatively large scatter in the correlation of halon-1211 and N₂O (Figure 10) is in part explained by a relatively large relative measurement uncertainty of halon-1211. Measured SF₆ is excluded from the mixing diagnosis because its mean relative measurement uncertainty is at least twice as large as those of the other species.

[26] A second parameter that is expected to influence the width of tracer-tracer correlations is the atmospheric lifetime (Table 2c). Species with a lifetime similar to that of N₂O, such as CF₂Cl₂ (CFC-12) and CCl₂FCClF₂ (CFC-113), have nearly linear correlations with N₂O (Figure 10). The near-linear correlation of CH₄ with N₂O indicates that it is also in this group. CH₃CCl₃ (MCF) is excluded because of its short atmospheric lifetime of about 5.2 years [Montzka *et al.*, 2000], leading in combination with its substantially reduced anthropogenic rate of production to a tropospheric growth rate of presently −14% per year [World Meteorological Organization, 1999; Anderson *et al.*, 2000]. The short lifetime results from comparatively large stratospheric rates of photolysis which may prevent MCF from develop-

ing tight correlations with long-lived tracers. CCl₄ is excluded because for 27 January 2000, measurements are not available.

[27] Midlatitude measurements taken above $\Theta = 465$ K do not fall onto the same correlation curves as the other measurements (Figure 10). This is evident for correlations of N₂O with halon-1211 and CFC-11, but also to a lesser degree for CFC-12 and CFC-113. The corresponding measurements stem from the midlatitude and transit flights, indicating that at these higher potential temperatures isentropic correlations differ from those describing the lower vortex. All flights sampling the polar vortex essentially measured the same correlations of long-lived tracers, indicating that the polar vortex is of a well-mixed nature. The mid-latitude points stemming from altitudes below 465 K populate and hence define the high-N₂O ends of the isentropic correlations. The measurements with $\Theta > 465$ K are excluded from the further analysis because the isentropic correlations corresponding to these points cannot be completely inferred from the ER-2 measurements. Envelopes representing the isentropic correlations are fitted to the remaining correlative tracer data (see Appendix B).



[28] For the analysis a knowledge of potential temperature along the flight tracks is necessary. Temperature and pressure (and hence potential temperature) along the flight tracks are measured by the Meteorological Measurement System (MMS) [Scott *et al.*, 1990]. The sharply defined minimum N_2O mixing ratio on every isentropic surface (Figure 10) marks the core of the vortex. At low isentropic surfaces N_2O attains its tropospheric background value of about 315 ppbv. Only above 400 K does the maximum N_2O mixing ratio fall off significantly. The corresponding data points result from the test and transit flights in mid-latitudes. The solid lines in the plot mark the bin boundaries ζ_k defining the step function H (section 2) as applied to the flights after 26 February. During the development of the vortex the core-vortex mixing ratios of N_2O decrease noticeably. Therefore for the flights before 3 February the dotted bin boundaries are assumed. The spacing of bin boundaries boundaries is discussed in section 6.4. The mixing analysis is restricted to points with $\Theta \geq 380$ K because when the isentropic tracer-tracer correlations are restricted to the interval of N_2O mixing ratios encountered below this surface, their respective curvature is essentially zero. In this situation a meaningful inversion of the mixing integral equation (1) is not feasible. For an analysis of mixing in the upper troposphere and lower stratosphere region a different set of more short-lived tracers would have to be chosen.

[29] The temporal resolution of N_2O , CFC-12, and halon-1211 of 70 seconds is degraded to match that of the other species of 140 seconds (Table 2). In total the SOLVE ER-2 missions yield about 1200 complete records of observations on which the diagnoses of mixing are based, consisting of the chemical tracers N_2O , CH_4 , CFC-11, CFC-12, CFC-113, and halon-1211, and of meteorological data along the flight tracks.

6.3. Interpolation of Model Data Onto the Flight Tracks

[30] For an optimal comparison of model and measurement data forward and backward isentropic trajectories are calculated, ending at the two nearest times for which the 24-hourly model data are available (the “analysis times”). At the two advected positions of the aircraft a linear interpolation of trace gas mixing ratios and bin amplitudes in λ , ϕ , and Θ is performed. Linear combinations of the two results, weighted with the temporal distance to the analysis times, give the final fields interpolated onto the flight tracks. The method has been used by *Morgenstern and Marenco* [2000]. Hence the bin amplitudes along the flight tracks result from first a calculation of bin amplitudes in the entire model domain and for the analysis times of interest and then an interpolation of the bin amplitudes onto the flight tracks. This is to avoid possible sampling problems.

6.4. Basic Model Performance

[31] Figure 11 shows a comparison of modeled versus measured tracers. Some deviations appear between modeled and measured N_2O . Above about 120 ppbv (i.e., for mid and low-latitude air) a substantial scatter is encountered.

Figure 9. (opposite) Product of mixing kernel amplitudes $H_2 \cdot H_4$ at 451 K from 22 February to 1 March 2000, at 4-day intervals.

Table 2. Species Measured by ACATS IV

	N ₂ O	CFC-12	CH ₄	CFC-113	CFC-11	SF ₆	CCl ₄	Halon-1211	MCF
Sampling intervals, ^a s	70	70	140	140	140	70	140	70	140
Approximate relative measurements uncertainties, %	0.3	0.5	0.5	0.5	0.4	2.8	0.6	1.4	0.9
Approximate atmospheric lifetimes, ^b years	120	100		80	50		40	20	5.2

^aData are missing about every 9 min to calibrate the ACATS instrument.

^bAfter *World Meteorological Organization* [1999] and *Montzka et al.* [2000]. For the lifetimes of CH₄ and SF₆, see text.

Moreover, the model systematically underestimates the measurements in this region. Below 120 ppbv, the reverse is true: The scatter is much reduced, and the model overestimates the measurements. Note that those measurements which form the tight correlation with the model data stem exclusively from the later flights after 26 February.

[32] CFC-11 has a significantly shorter lifetime in the stratosphere than N₂O, resulting in a different balance between subsidence, chemistry, and mixing in the vortex. Erroneous rates of subsidence are here not as important as for N₂O since even a slow subsidence will bring nearly completely depleted air to the flight level. This leads to a better agreement between the model and the measurements than for N₂O. The tight correlation in the vortex (below about 30 pptv of CFC-11) is likewise evident. A similar argument holds for halon-1211 with its even shorter lifetime. Outside the polar vortex the model also systematically underestimates the halon-1211 measurements since the regression parabola is above the diagonal everywhere except in the vortex. Of all four tracers, N₂O has the most significant deviation from a linear correlation between the modeled and measured species.

[33] Since the bin boundaries for the analysis of mixing (section 2) are based on the mixing ratios of N₂O, the systematic deviations between the model and the measurements need to be accounted for in the determination of bin boundaries. For the model data the bin boundaries are here chosen to be equidistant in modeled N₂O and span the entire range of mixing ratios of N₂O encountered north of 35°N on an isentropic surface. Let $p_2(\zeta)$ be the regression parabola that relates measured to modeled N₂O (Figure 11). Instead of choosing bin boundaries equidistant in measured tracer space of N₂O, they are chosen to be equidistant in the respective modeled N₂O, assuming that the relation is given by p_2 . The result is displayed in Figure 10; the middle bin boundaries are shifted to higher mixing ratios with respect to an equidistant distribution. The outer bin boundaries ζ_0 and ζ_5 are unaffected.

6.5. Analysis of Two Individual Flights

[34] On 27 January en route between Kiruna and Russia and back the boundary of the polar vortex was crossed twice (Figure 12). Pronounced gradients in the measured tracers (labeled “A” and “D”) suggest that the vortex boundary was encountered shortly after 1000 UTC and again at 1300 UTC. (The labels B and C denote a dive and subsequent ascent after 1200 UTC.) Generally the model follows the evolution of the tracers well but does not reproduce the steep gradients of the measurements at the edge. Modeled halon-1211 underestimates the measurements in midlatitudes, as noted in section 6.4. The determination of the H_k is unaffected by this problem.

[35] A comparison of the mixing kernels derived from the model and measurement data (Figure 13) indicates that

broadly the model and the measurements agree that, at the beginning and end of the flight, core-vortex air (H_0) was encountered, while in the middle some midlatitude air was sampled. The transition through the bins is more gradual in the model, compared to the measurements. Bin H_1 is encountered twice in the model but skipped almost completely in the measurements. At around 1020 and again around 1300 UTC (labels A and D) the model suggests an overlap (i.e., mixing) between H_0 and H_2 . The measurements confirm this finding though during the second transition the mixture is encountered slightly earlier in the measurements than in the model.

[36] The second flight toward midlatitudes took place on 11 March 2000. Along the flight route from Kiruna toward northern Scotland and back a filament forming at the edge of the polar vortex was crossed twice. It is characterized by a horizontal layering of midlatitude and polar-vortex air. A comparison of model and measurements (Figure 14) again confirms that N₂O, CFC-11, and SF₆ are closely reproduced by the model, while halon-1211 has somewhat larger discrepancies in midlatitudes, paralleling the findings for the flight of 27 January. The filament labeled “A” and “D” has a stronger signature in the measurements than in the model. The model overestimates N₂O inside the vortex. This suggests that subsidence inside the vortex, bringing N₂O-

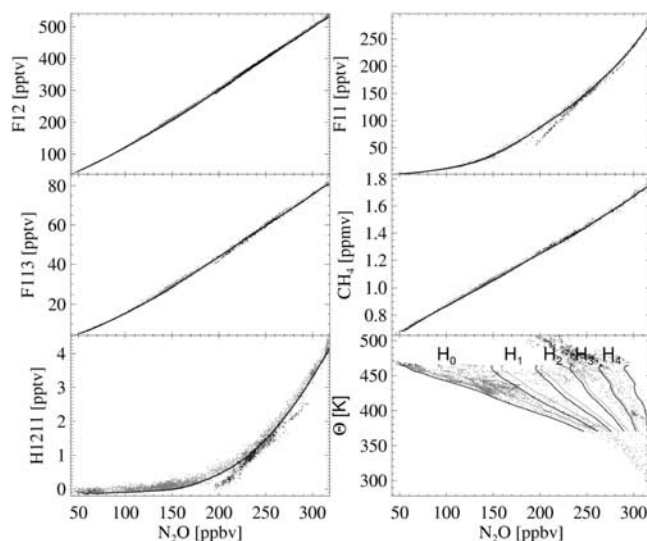


Figure 10. Correlative plots of N₂O versus CFC-12, CFC-11, CFC-113, CH₄, halon-1211, and Θ , for all ER-2 SOLVE/THESEO 2000 flights. Red dots denote measurements with $\Theta \leq 465$ K, black dots denote those with $\Theta > 465$ K. The black solid lines denote the outer envelopes $\Psi_i(\zeta)$. On the N₂O- Θ plot are superimposed the boundaries ζ_k corresponding to the “bins” H_0 to H_4 (see text). See color version of this figure at back of this issue.

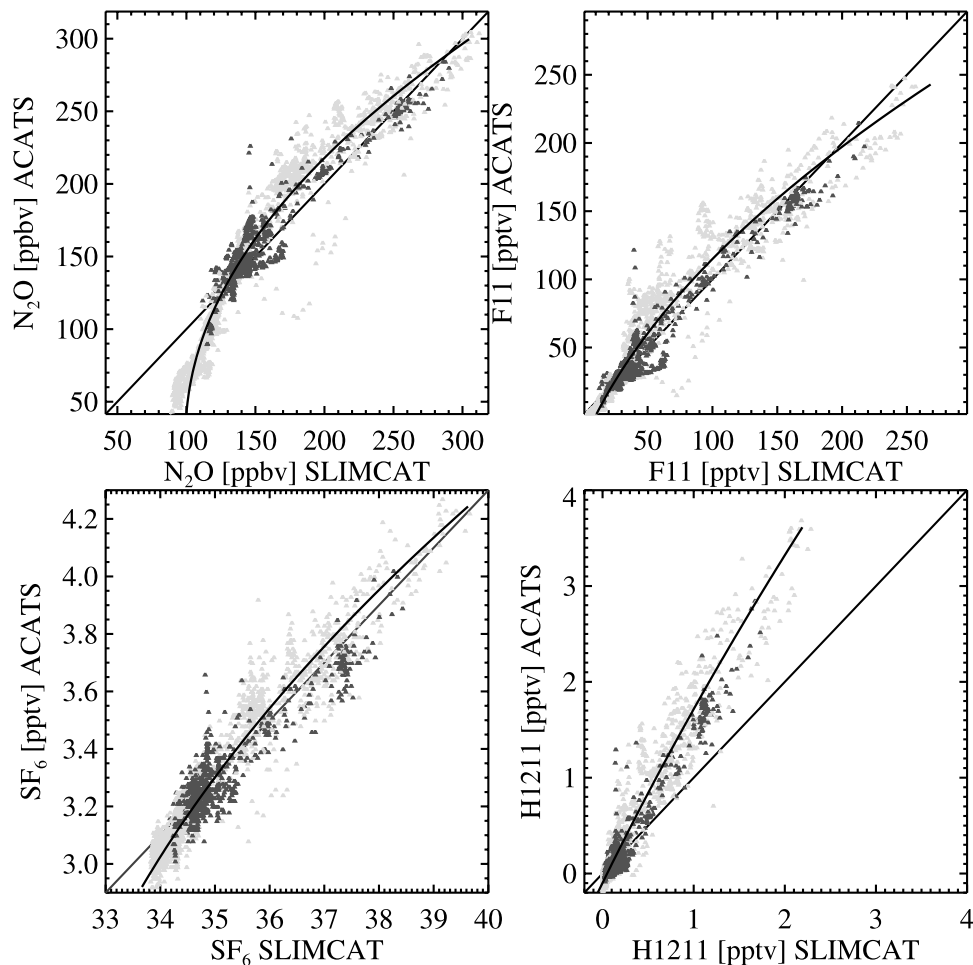


Figure 11. Modeled versus measured mixing ratios for N_2O , CFC-11, halon-1211, and SF_6 (arbitrary units in SLIMCAT). Red symbols depict measurements taken between 9 January and 3 February 2000, yellow symbols depict those between 26 February and 16 March. The solid lines denote the diagonals and the regression parabolas. See color version of this figure at back of this issue.

depleted air to the flight altitude, is too slow in the model. The effect is not seen in CFC-11 and halon-1211 because the vortex air is almost completely depleted of these tracers by the time it arrives at the flight altitude.

[37] The mixing analysis (Figure 15) confirms that a filament was encountered upon crossing the boundary of the polar vortex, at about 0930 UTC and again at 1215 (labels A and D). The measurements suggest that the filament was slightly further south than placed by the model. The positions of the vortex edge (crossed at about 0910 and 1240 UTC) are in good agreement, and so are generally the amplitudes H_k . Both agree that there was mixing of inner- and boundary-vortex air (i.e., an overlap of the bins H_0 and H_2) on the mid-latitude side of the polar vortex edge.

7. Discussion

[38] The analysis presented above uses different tracers for the diagnosis of mixing in the ER-2 measurements, compared to the model. However, mixing is similar in both cases, indicating that the choice of tracers may be varied with little effect on the results, provided that the tracers span

a range of sufficiently different photochemical behaviors so that their isentropic tracer-tracer correlations with a reference tracer are linearly independent. Mixing in the measurements is somewhat overdetermined, so individual tracers may be omitted from the analysis. This again leaves the results largely unchanged.

[39] In its present form the method requires the diagnostic determination of “correlation envelopes” that uniquely map one tracer onto another on an isentropic surface. In the SLIMCAT integration, if tropical data points are included, the data fall onto two distinct branches that make such a mapping impossible (Figure 1). An investigation of tropical measurements would be necessary to examine whether it is a model artefact; this is however beyond the scope of this paper. If it is not a model artefact, or indeed for this version of SLIMCAT, it limits the applicability of the method.

[40] Mixing is diagnosed in terms of a mixing kernel, which is approximated by the step function H . By the nature of the method details of the results depend on the position and number of bin boundaries ζ_k chosen to represent H . A variation of the bin boundaries results in a different distribution of amplitudes over the different bins, H_k . The spacing of bins is selected to cover the

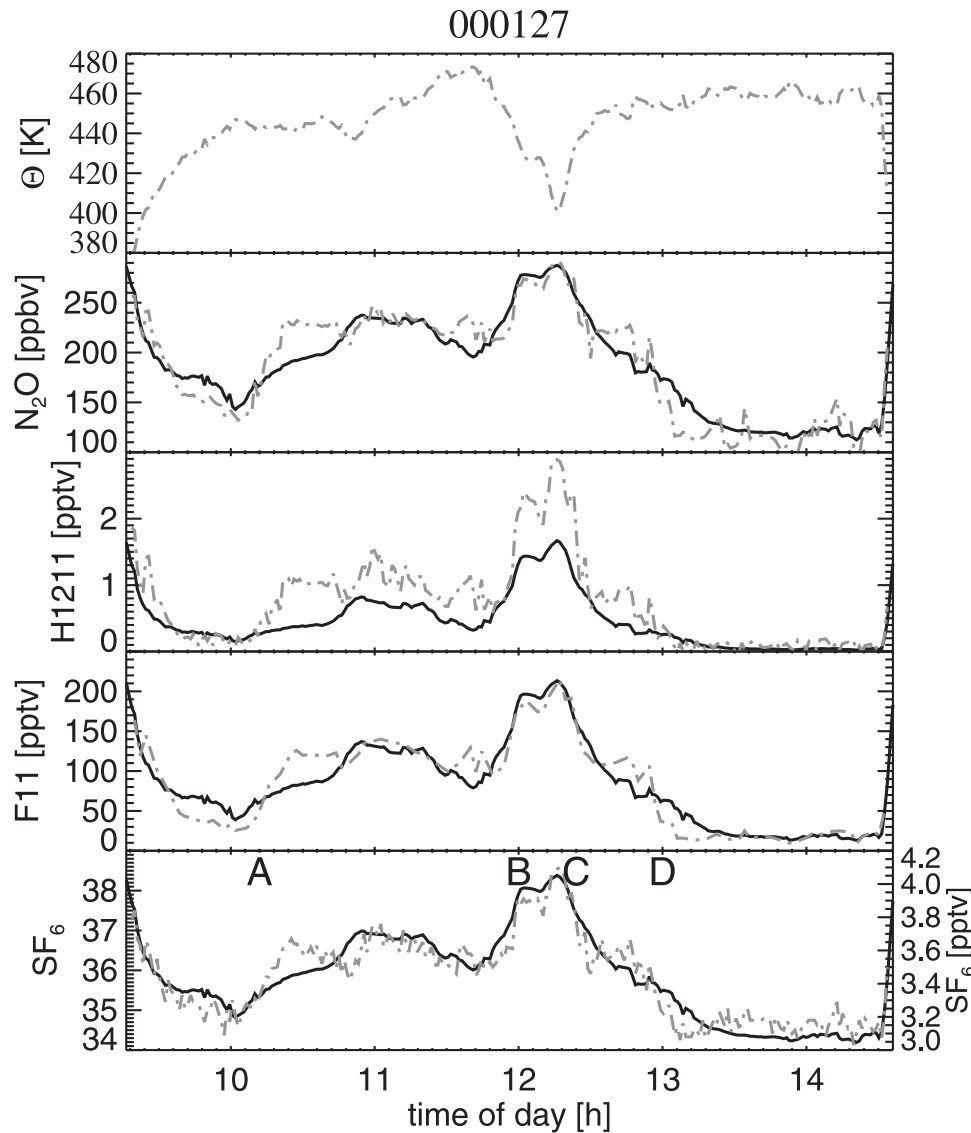


Figure 12. Θ , N_2O , halon-1211, CFC-11, and SF_6 (in the model: arbitrary units) along the flight track of 27 January 2000. Solid: Model interpolates. Dash-dotted: measurements. The right scale applies to the SF_6 measurements.

variability of the reference tracer N_2O in the region of interest, the polar vortex to midlatitudes. Given the amount of information available in the measured tracer data, an increase in the number of bins is mathematically possible but does not produce significant further insight. (For the model data, with no further assumptions an increase is not possible; see section 2.) Appendix C contains a sensitivity study in which H is chosen to be continuous and piecewise linear. The result supports the view that if a data point is some distance away from the isentropic correlation, the method will produce an overlap of distant bins, almost irrespectively of where the bin boundaries are placed and which approximation is chosen to represent h . In this respect the diagnosis of mixing is robust with respect to sensible variations of these parameters.

[41] A further assumption is that the signs of curvature of isentropic correlations do not change so that outer and inner sides of the curves may be defined. We argue that in the presence of a single transport barrier a change of the sign of

curvature cannot occur because mixing on either side of the barrier straightens out the isentropic correlation while a single kink occurs at the position of the barrier. With a second transport barrier a change of the sign of curvature would be possible. In the cases considered here, changes in the sign of curvature of the isentropic correlations do not occur. The method does not explicitly require any particular sign of curvature of the tracer-tracer correlations. Here all correlations are positively curved, but the method would equally work with negative curvature, or indeed with negatively correlated tracer pairs.

[42] A fraction of mixing occurs locally in tracer space, i.e., it does not involve bringing air masses from very different parts of tracer space together. Instead, parcels neighboring in tracer space are perpetually mixed, adding to the compactness of isentropic correlations. *Plumb et al.* [2000] call this type of mixing “regular”. In the version presented here, due to insufficient numerical sensitivity, the formalism cannot capture regular mixing (section 2). This

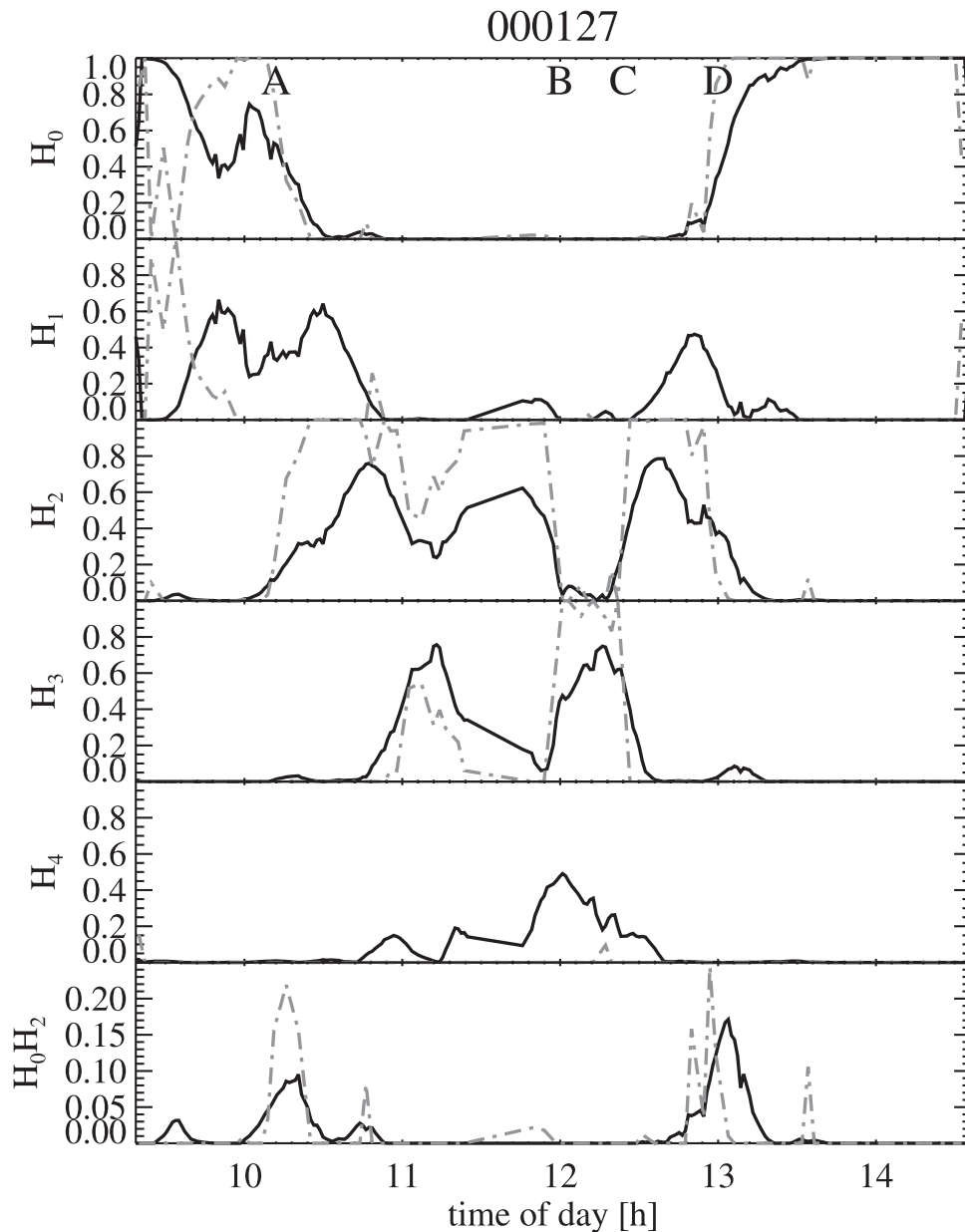


Figure 13. The mixing kernel amplitudes H_0 to H_4 and their product H_0H_2 along the flight track of 27 January 2000. Solid: derived from the model. Dash-dotted: derived from measurements.

constitutes a limitation of the method. Sustained local mixing can lead to the formation of air parcels with more than two origins in tracer space, in which case the conventional “mixing line” approach leads to erroneous conclusions about the origins of such air parcels. In principle the method presented here would treat such situations correctly since it explicitly generalizes the mixing of exactly two points in tracer space, although in the present form a sufficient spacing of origins is necessary.

[43] Diabatic effects may change isentropic correlations in competition with mixing, and differential diabatic heating in midlatitudes may broaden isentropic correlations. The change of isentropic correlations due to subsidence in the vortex is accounted for by recomputing the correlation envelopes at every time mixing is calculated. Performing a trajectory study, *Sparling et al.* [1997] show

that parcels that start out on a single isentropic surface experience substantial diabatic dispersion in the latitude $-\Theta$ plane. A determination of exactly how much this effect influences our results would require a separate study because of the different choice of analyses used here, the way diabatic motion is specified, and the fact that the diabatic dispersion obtained by *Sparling et al.* [1997] contains a reversible component due to meteorological dynamics.

[44] In addition to diabatic effects, chemistry changes isentropic tracer-tracer correlations. The lifetimes of tracers considered here range between 20 and 120 years (Table 2c). Even though equivalent stratospheric lifetimes, reflecting for example the average rates of photochemical loss at the considered altitudes, may be an order of magnitude smaller (e.g., *Minschwaner et al.* [1996] report a photochemical

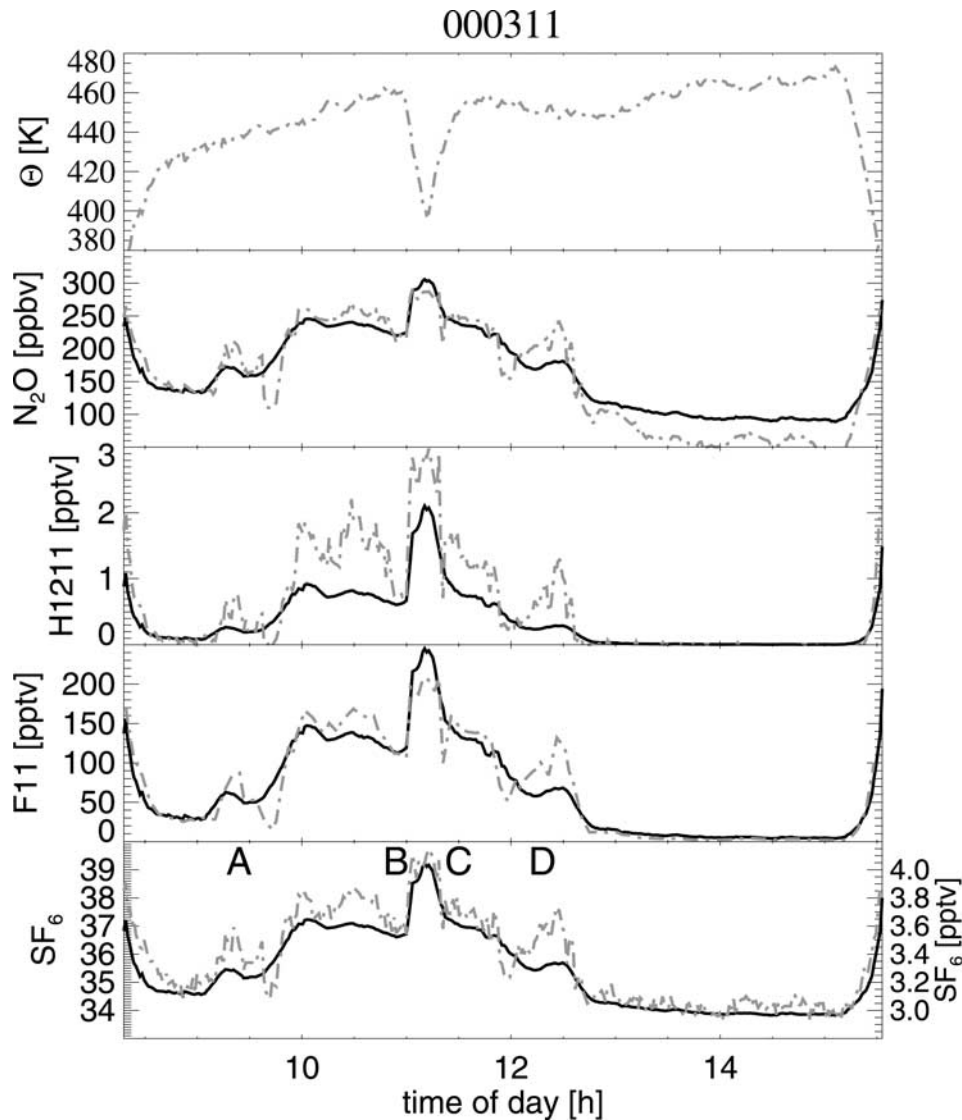


Figure 14. Θ , N_2O , halon-1211, CFC-11, and SF_6 along the flight track of 11 March 2000. Solid: Model interpolates. Dash-dotted: Measurements.

lifetime of 1 year for CFC-11 at 22 km in the tropics), they are not on the timescale of planetary waves responsible for mixing. Hence chemistry is thought to play a minor role here, but of course is essential in setting up the observed or modeled tracer-tracer correlations over longer periods of time. In some situations an inclusion of odd nitrogen or water vapor may be desirable but denitrification and dehydration would need to be accounted for carefully.

[45] As a note of caution, strictly the model analysis only shows that in the model filaments often have an anomalous composition indicative of mixing. However, in reality mixing presumably occurs at scales below those resolved by the models [e.g., Morgenstern and Carver, 1999, 2001, and references therein]. Hence an underlying assumption in transferring the results to the real atmosphere must be that the rate of filamentation in the models is similar to reality, because it is forced by the large-scale flow, and that filamentation is the rate-limiting step. In that case, the precise scale which diffusive mixing occurs at may be of

little relevance as far as gross transport of long-lived species across the vortex boundary is concerned. For short-lived tracers, by contrast, it can have a substantial impact [Thuburn and Tan, 1997; Searle et al., 1998]. A discussion of the real nature of mixing, involving an analysis of the fractal distribution of scales in stratospheric measurements [e. g., Tuck and Hovde, 1999], is beyond the scope of this paper.

[46] When applying the method to observations, the assumption is made that the correlation discerned from the measurements is indeed an isentropic correlation describing correlations in the region between the polar vortex and midlatitudes. A dependence of those functions on Θ cannot be discerned for points below 465 K but is clearly visible at higher isentropic levels. The assumption also depends on whether the measurements capture tracer-tracer variability on both sides of the polar vortex boundary. This appears to be the case, given the tight correlations of relatively reactive tracers like CFC-11 with N_2O (Figure 10). A change of tracer-tracer correlations between early and late flights of

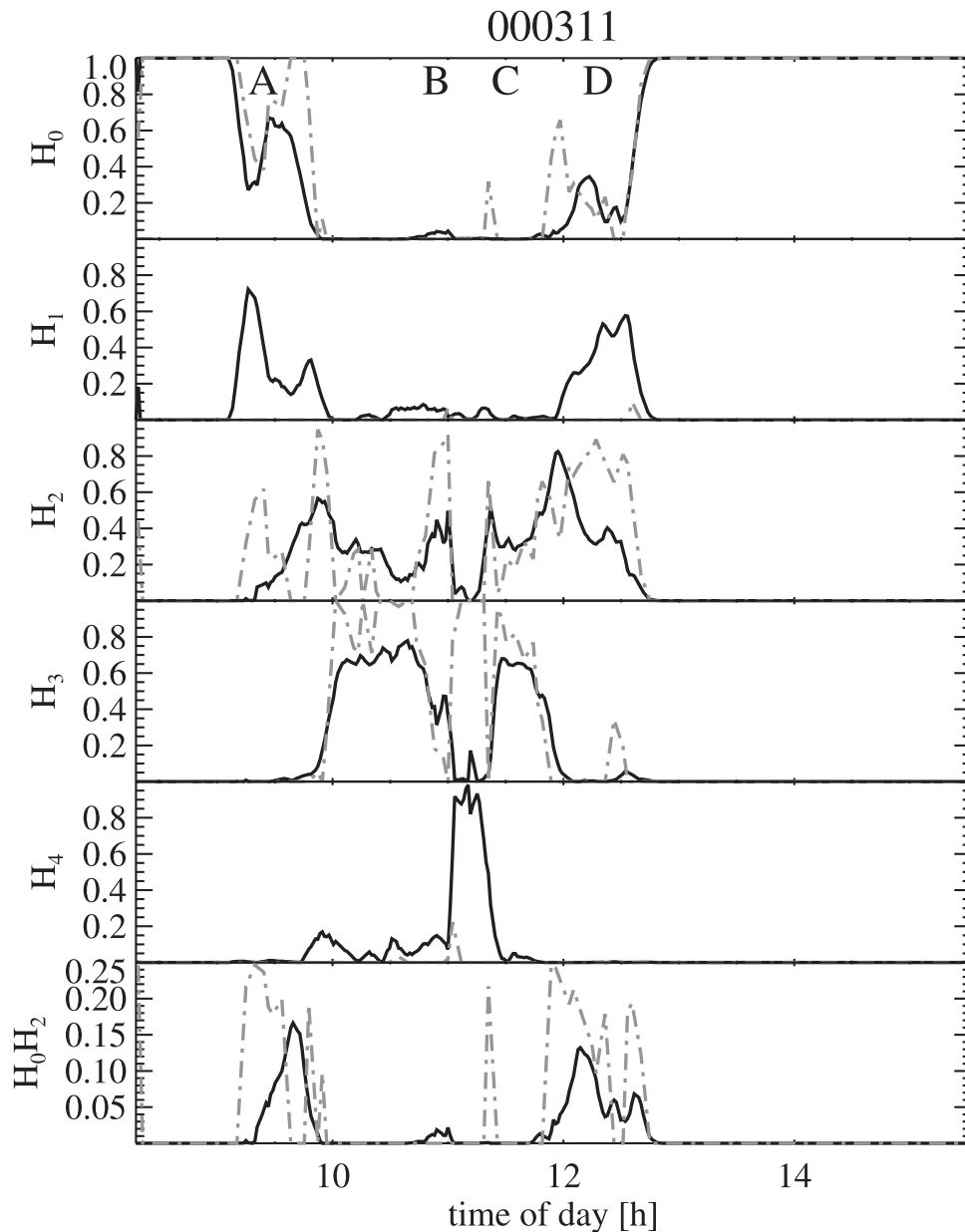


Figure 15. Θ , the mixing kernel amplitudes H_0 to H_4 , and their products H_0H_2 along the flight track of 11 March 2000. Solid: derived from the model. Dash-dotted: derived from measurements.

the campaign is not evident, suggesting that transport across the vortex boundary has not appreciably modified the composition of the vortex at the flight altitude in the intervening period. For the two flights analyzed here, an interleaving of vortex and extra-vortex air was found, similar to the findings of *Murphy et al.* [1989]. This supports the view that the boundary of the polar vortex is of a finite width and there is transport from the boundary of the polar vortex to midlatitudes and vice versa. The finding is largely in agreement with *Tuck* [1989], who suggests active exchange below 400 K and a suppression of isentropic exchange above this level over Antarctica, though the transition level may be at a higher potential temperature in the Arctic.

[47] The method will be modified in a forthcoming publication to assess cumulative mixing and possibly

“mixing timescales” in the sense of *Minschwaner et al.* [1996].

8. Summary

[48] A method has been developed to quantify mixing from a suite of long-lived tracers. The method relies on the tracers forming tight, curved correlations with a reference tracer (here N_2O) on an isentropic surface. Under such circumstances “isentropic correlations” are given as the outer envelope functions bounding a large set of isentropic data points in tracer space. In a generalization of the established concept of “mixing lines”, mixing is viewed as resulting from a convolution of the correlation envelopes, involving a mixing kernel H . The number of degrees of freedom H can have depends on the number of tracers with

a photochemical behavior sufficiently different from that of the other tracers to allow an independent correlation with a reference tracer to develop. The method is applied to two episodes simulated using the SLIMCAT chemical transport model, and to measurements taken during two ER-2 flights of the SOLVE/THESEO 2000 campaign. In all cases the method singles out data points with an anomalous composition in tracer space, and mixing diagnosed from the measurements broadly agrees with that of the model. The occurrence of anomalous data points is linked to filamentation and hence to mixing across the boundary of the polar vortex. The method gives quantitative information about the origins of an air mass prior to a mixing event, allowing for multiple origins. In this respect it constitutes a further development over and above the conventional “mixing lines” approach as reviewed by *Plumb et al.* [2000]. In comparison with this conventional approach, the method as defined here explicitly addresses the problem of multiple origins of an air parcel following a mixing event. However, the method is limited to mixing which is sufficiently long-range in tracer space. In the presence of multiple tracer measurements the traditional approach may theoretically lead to conflicting results about origins of air parcels, while our method explicitly requires a set of multiple tracer measurements or model data. This makes the method a useful tool for the analysis of multiple tracer data.

Appendix A: Details of the Inversion Procedure

[49] Equation (2) constitutes a linear optimization problem. The solution is obtained in a series of steps detailed here. For a list of notations, see notation section.

1. All tracers are rescaled such that on a given isentropic surface the grid point mean tracer mixing ratio equals their total atmospheric lifetime in the case of model data, and their mean relative measurement accuracy in the case of measurements. Both are listed in Table 2. The atmospheric lifetime provides a measure of confidence to which degree a spread in tracer-tracer correlations can be attributed to mixing and not photochemistry. For the inert model tracer SF₆ a weight of 35 years is assumed approximately reflecting its relative tropospheric growth rate in the model. The results show little sensitivity to the choice of weights.

2. Outer envelopes $\Psi_i(\zeta)$ are determined from the pairs of correlative tracer data (see Appendix B).

3. To remove redundant information from the data, an orthogonalization procedure is applied to both the correlation envelopes and the original tracer data. Let $\langle \cdot, \cdot \rangle$ denote the function inner product $\langle \Phi, \Psi \rangle = \int \Phi(\zeta) \Psi(\zeta) d\zeta$. “Orthogonal tracers” ψ'_i and envelopes Ψ'_i are introduced as linear combinations of original tracers according to the prescriptions

$$\Psi'_i = \Psi_i - \sum_{j=0}^{i-1} \frac{\langle \Psi_i, \Psi'_j \rangle}{\langle \Psi'_j, \Psi'_j \rangle} \Psi'_j \quad (\text{A1})$$

and

$$\psi'_i = \psi_i - \sum_{j=0}^{i-1} \frac{\langle \Psi_i, \Psi'_j \rangle}{\langle \Psi'_j, \Psi'_j \rangle} \psi'_j. \quad (\text{A2})$$

The new envelopes satisfy $\langle \Psi'_i, \Psi'_j \rangle = 0$ for $i \neq j$. Here $\Psi'_0 = \Psi_0 \equiv 1$ denotes the “normalization” tracer and $\Psi_1 \sim \zeta$, the reference tracer N₂O. Note that potential additional tracers entering the analysis only add new information if after the orthogonalization procedure their correlation envelope is distinguishable from computational noise, or in chemical terms the photochemical behavior needs to be sufficiently different from those of the other tracers.

4. Let $H(\zeta; \mathbf{x}, t) = \sum_{k=0}^{m-1} H_k(\mathbf{x}, t) s_k(\zeta; \Theta, t)$ be the step function depicted in Figure 3c. The s_k 's are defined as rectangular functions with respect to the nodes $\zeta_k(\Theta, t)$:

$$s_k(\zeta; \Theta, t) = \begin{cases} 1/(\zeta_{k+1} - \zeta_k) & \text{for } \zeta_{k+1} \geq \zeta > \zeta_k, \\ 0 & \text{otherwise,} \end{cases} \quad (\text{A3})$$

normalized such that $\langle s_k, 1 \rangle = 1$. The inversion of the mixing problem then consists of minimizing with respect to H the “cost functional” $f(H) = \sum_{i=1}^p (\psi'_i - \langle H, \Psi'_i \rangle)^2$ under the conditions $H \geq 0$ and $\langle H, 1 \rangle \equiv \sum_{k=0}^{m-1} H_k = 1$. Steps 1, 3, and 4 amount only to a specification of the norm in equation (1). See sections 5.1 and 6.2 and Appendix C for discussions of the choices of bin boundaries. A different approximation is tested in Appendix C.

5. Let $\mathbf{C} = (c_{ki}) = (\langle s_k, \Psi'_i \rangle)$ be a matrix, and $\mathbf{n} = (\langle s_k, 1 \rangle)$ be a normalization vector, then equation (2) is equivalent to the linear problem $f(\mathbf{h}) = |\psi' - \mathbf{C}\mathbf{h}|^2$ under the conditions $\mathbf{h} \geq 0$ and $\mathbf{h} \cdot \mathbf{n} = 1$. This is a standard problem of optimization theory solved using the “simplex algorithm” because the inequality $\mathbf{h} \geq 0$ means that the space of solutions is bounded by hyperplanes and hence is a multidimensional polygon (i.e., a simplex).

[50] Let m be the dimensionality of \mathbf{h} ($m = 5$ here). Let $\mathcal{K} = \{k_1, \dots, k_q\} \subset \mathcal{L} = \{0, \dots, m-1\}$ such that \mathbf{h} is zero with respect to indices not in \mathcal{K} , i.e., $h_{\mathcal{L}/\mathcal{K}} = 0$. Let $\mathbf{b} = h_{\mathcal{K}}$ be the reduction of \mathbf{h} that is allowed to take nonzero values, likewise $\mathbf{e} = \mathbf{n}_{\mathcal{K}}$ and $\mathbf{E} = (c_{ki})$; \mathbf{b} is decomposed into a projection parallel and one perpendicular to \mathbf{e} : $\mathbf{b} = \mathbf{b}_{\parallel} + \mathbf{b}_{\perp}$. Then

$$\mathbf{b}_{\parallel} = \mathbf{e}/|\mathbf{e}|^2 \quad (\text{A4})$$

satisfies $\mathbf{b}_{\parallel} \cdot \mathbf{e} = 1$. Let now $\mathcal{B} = \{\mathbf{b}_{\parallel}, \mathbf{b}_2, \dots, \mathbf{b}_q\}$ be a basis such that $\mathbf{b}_{\parallel} \cdot \mathbf{b}_i = 0$ for $i = 2, \dots, q$. Let $\mathbf{G} = (\mathbf{b}_2, \dots, \mathbf{b}_q)$. Then

$$\mathbf{b} = \mathbf{b}_{\parallel} + \mathbf{G}\mathbf{r} \quad (\text{A5})$$

with any choice of \mathbf{r} satisfies $\mathbf{b} \cdot \mathbf{e} = 1$. The cost function becomes

$$f(\mathbf{r}) = |\psi' - \mathbf{E}(\mathbf{b}_{\parallel} + \mathbf{G}\mathbf{r})|^2 \equiv |-\mathbf{U}\mathbf{r}|^2, \quad (\text{A6})$$

which is minimized by $\mathbf{r} = (\mathbf{U}^T\mathbf{U})^{-1}\mathbf{U}^T\mu$ and

$$\mathbf{b} = \mathbf{e}/|\mathbf{e}|^2 + \mathbf{G}(\mathbf{U}^T\mathbf{U})^{-1}\mathbf{U}^T(\psi' - \mathbf{E}\mathbf{e}/|\mathbf{e}|^2). \quad (\text{A7})$$

\mathbf{r} and \mathbf{b} are acceptable if $\mathbf{b} \geq 0$. Repeat the procedure for all nonempty subsets $\mathcal{K} \subset \mathcal{L}$; the overall solution is then given by the one that yields the smallest of all values for f . There are $2^m - 1$ such subsets. In the examples considered in the

$H_1 \cdot H_3 @ 451K 00030112$

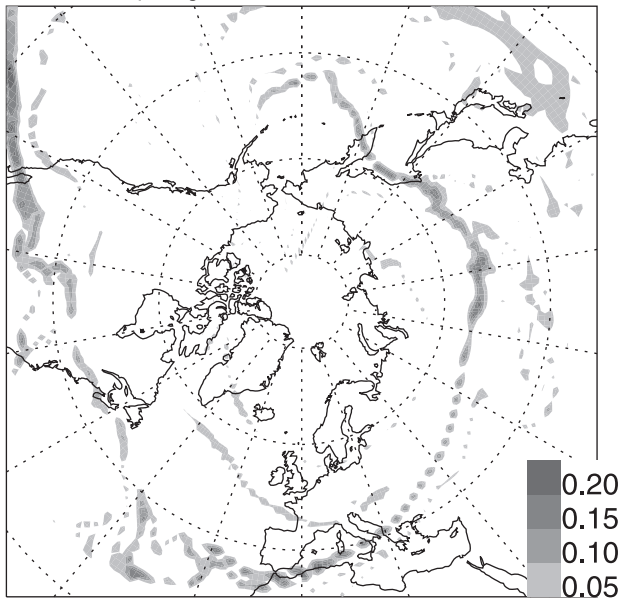


Figure C1. Same as Figure 9, but for the product $H_1 H_3$ of Appendix C for 1 March 2000, 12 UTC. See text for details.

text, in most cases the number of nonzero bins q equals 1, 2, or 3, meaning that the minimization problem is usually overdetermined and hence well posed.

Appendix B: Determination of Envelopes

[51] The envelopes Ψ_i are determined in three steps:

1. An inspection of the measured tracer-tracer correlations (Figure 10) reveals that for some tracers such as halon-1211 the outer edge of the correlative data set with N_2O , which the method requires to be sharply defined, is somewhat blurred, presumably reflecting measurement uncertainties. It is therefore necessary to prevent such anomalous points from dominating the computation of the outer envelope, Ψ_i , in the case of measurements. A 4th-order regression polynomial is fitted to the correlative tracer data. Then an ϵ -strip is defined that contains the regression polynomial in its centre. ϵ is determined such that 90% of the data points are contained within the strip and 5% outside of it on either side. Those points lying outside the strip are then suppressed for the computation of the envelope. In the case of model data, this step is omitted (e.g., Figure 1).

2. A regression parabola is fitted to the remaining data. The curvature term of the regression parabola determines whether the correlation is considered to be positively (negatively) curved.

3. The interval of N_2O values is subdivided into 200 equal-sized subintervals; on every subinterval the minimum (maximum) of tracer values defines the isentropic correlation curve.

[52] Given that by far most model data points lie close to the envelope (Figure 1), thinning the model data within reasonable limits to simulate observations would not change the resulting correlation envelopes much. If the Ψ_i are determined from observations, Figure 10 suggests that in the cases of sufficiently long-lived tracers the resulting

correlation envelopes are very close to a regression function resulting from the measurements. The only exception is the short-lived compound halon-1211, whose correlation with N_2O exhibits more scatter than in the other cases. This may be largely explained by its measurement uncertainty; correspondingly, halon-1211 carries less weight than the other tracers.

Appendix C: Different Approximation to the Mixing Kernel

[53] Choosing a piecewise constant approximation to the mixing kernel $h(\zeta)$ (like in section 2) is not the only possibility. In this section, H is chosen to be piecewise linear with respect to a set of nodes, ζ_k , i.e., $H(\zeta) = \sum_k H_k s_k(\zeta)$, where the s_k describe triangular functions in ζ , centered at ζ_k , with $\langle s_k, 1 \rangle = 1$. The result of a computation equivalent to section 5.2, but with the nodes placed at 90, 73, 57, 40, and 0° of equivalent N_2O latitude, is shown in Figure C1. The filament is diagnosed in the same position as before, but the distribution of origins changes with the different positions of the “bins” used here. Qualitatively the result is not very sensitive to the choice of bins and the details of the approximation. The diagnosis presented here indicates mixing of the bins peaking at 73 and 40°, while in section 5.2 is seen to involve the regions 60–70° and 0–40°. Given the finite widths of the triangular basis functions considered here, the two results corroborate each other, in spite of the different enumeration of the bins in the two variants.

Notation

$\Psi'_i(\zeta)$	orthogonalized isentropic correlation; equation (A1)
$\langle \dots \rangle$	function inner product $\langle \chi, \xi \rangle = \int \chi(\zeta) \xi(\zeta) d\zeta$
λ	longitude
μ	$= \psi' - \mathbf{E} \mathbf{b}_{\parallel}$; equation (A6)
ϕ	latitude
ψ_i	long-lived tracer data
ψ'_i	“orthogonalized” tracer data; equation (A2)
ψ'	$= (\psi'_i)$; vector of ψ'_i
$\Psi_i(\zeta)$	isentropic correlation function
$\Psi'_i(\zeta)$	orthogonalized isentropic correlation; equation (A1)
Θ	potential temperature
ζ	reference tracer (N_2O) mixing ratio
ζ_k	values of ζ defining intervals for H
\mathbf{b}	$= \mathbf{h}_{\zeta}$; nonzero reduction of \mathbf{h}
\mathbf{b}_{\parallel}	$= \mathbf{e}/ \mathbf{e} $; component of $\mathbf{b} \parallel \mathbf{e}$; equation (A4)
\mathbf{b}_{\perp}	$= \mathbf{G} \mathbf{r}$; component of $\mathbf{b} \perp \mathbf{e}$; equation (A5)
\mathcal{B}	$= \{\mathbf{b}_{\parallel}, \mathbf{b}_1, \dots, \mathbf{b}_{q-1}\}$; $\mathbf{b} \in \text{span}(\mathcal{B})$
\mathbf{C}	$= (\langle s_k, \Psi'_i \rangle)$, “mixing matrix”
\mathbf{e}	$= \mathbf{n}_{\zeta}$
\mathbf{E}	$= (c_{\zeta i})$
$f(H)$	“cost functional” to be minimized; equation (2)
\mathbf{G}	$= (\mathbf{b}_1, \dots, \mathbf{b}_{q-1})$; matrix of basis vectors $\perp \mathbf{b}_{\parallel}$
$\Psi'_i(\zeta)$	orthogonalized isentropic correlation; equation (A1)
$h(\zeta)$	mixing kernel; equation (1)
$H(\zeta)$	$= \sum_{k=0}^{q-1} H_k s_k(\zeta)$; approximation to h , equation (2)
H_k	components of \mathbf{h} and amplitudes of H
\mathbf{h}	(H_k) ; vector notation of H
i, j	indices for chemical species

k index for the different regions of origin (“bins”)
 $\mathcal{K} \subset \mathcal{L}$; bins of nonzero amplitude
 $\mathcal{L} = \{0, \dots, m-1\}$; bin indices
 $m \leq p+1$; number of bins
 $\mathbf{n} = (\langle s_k, 1 \rangle)$; normalization vector of the s_k
 p number of tracers
 $q \leq m$; number of bins of nonzero amplitude
 \mathbf{r} vector of coefficients in span (B)
 $s_k(\zeta)$ rectangular basis functions; equation (A1)
 t time
 $\mathbf{U} = \mathbf{E}\mathbf{G}$; equation (1)
 $\mathbf{x} = (\lambda, \phi, \Theta)$, vector of spatial coordinates.

[54] **Acknowledgments.** Martyn Chipperfield is acknowledged for making his model available. The British Atmospheric Data Centre is acknowledged for providing access to the ECMWF analyses. OM is supported by the European Commission under grant EUK2-CT-1999-CO049 within the SAMMOA project. We acknowledge support by the U.K. Natural Environment Research Council (NERC) within the U.K. Universities Global Atmospheric Modelling Programme (UGAMP). The Centre for Atmospheric Science is a joint initiative of the Departments of Applied Mathematics and Theoretical Physics and of Chemistry.

References

- Anderson, J., J. M. Russell III, S. Solomon, and L. E. Deaver, Halogen Occultation Experiment confirmation of stratospheric chlorine decreases in accordance with the Montreal Protocol, *J. Geophys. Res.*, *105*, 4483–4490, 2000.
- Chipperfield, M. P., Multiannual simulations with a three-dimensional chemical transport model, *J. Geophys. Res.*, *104*, 1782–1805, 1999.
- Elkins, J. W., et al., Airborne gas chromatograph for in situ measurements of long-lived species in the upper troposphere and lower stratosphere, *Geophys. Res. Lett.*, *23*, 347–350, 1996.
- Fahey, D. W., et al., A diagnostic for denitrification of the winter polar stratosphere, *Nature*, *345*, 698–702, 1990.
- Goldan, P. D., W. C. Kuster, D. L. Albritton, and A. L. Schmeltekopf, Stratospheric CFCl_3 , CF_2Cl_2 , and N_2O height profile measurements at several latitudes, *J. Geophys. Res.*, *85*, 413–423, 1980.
- Haynes, P. H., and E. F. Shuckburgh, Effective diffusivity as a diagnostic of atmospheric transport, I, Stratosphere, *J. Geophys. Res.*, *105*, 22,777–22,794, 2000.
- Kelly, K. K., et al., Dehydration in the lower Antarctic stratosphere during late winter and early spring, 1987, *J. Geophys. Res.*, *94*, 11,317–11,357, 1989.
- Michelsen, H. A., et al., Correlations of stratospheric abundances of CH_4 and N_2O derived from ATMOS measurements, *Geophys. Res. Lett.*, *25*, 2777–2780, 1998.
- Minschwaner, K., A. E. Dessler, J. W. Elkins, C. M. Volk, D. W. Fahey, M. Loewenstein, J. R. Podolske, A. E. Roche, and K. R. Chan, Bulk properties of isentropic mixing into the tropics in the lower stratosphere, *J. Geophys. Res.*, *101*, 9433–9439, 1996.
- Montzka, S. A., et al., New observational constraints for atmospheric hydroxyl on global and hemispheric scales, *Science*, *288*, 500–503, 2000.
- Morgenstern, O., and G. D. Carver, Quantification of filaments penetrating the subtropical barrier, *J. Geophys. Res.*, *104*, 31,275–31,286, 1999.
- Morgenstern, O., and G. D. Carver, Comparison of cross-tropopause transport and ozone in the upper troposphere and lower stratosphere region, *J. Geophys. Res.*, *106*, 10,205–10,221, 2001.
- Morgenstern, O., and A. Marengo, Wintertime climatology of MOZAIC ozone based on the potential vorticity and ozone analogy, *J. Geophys. Res.*, *105*, 15,481–15,493, 2000.
- Murphy, D. M., A. F. Tuck, K. K. Kelly, K. R. Chan, M. Loewenstein, J. R. Podolske, M. H. Proffitt, and S. E. Strahan, Indicators of transport and vertical motion from correlations between in situ measurements in the Airborne Antarctic Ozone Experiment, *J. Geophys. Res.*, *94*, 11,669–11,685, 1989.
- Piani, C., W. A. Norton, A. M. Iwi, E. A. Ray, and J. W. Elkins, Transport of ozone depleted air on breakup of the stratospheric polar vortex in spring/summer 2000, *J. Geophys. Res.*, *107*, 10.1029/2001JD000488, in press, 2002.
- Plumb, R. A., A “tropical pipe” model of stratospheric transport, *J. Geophys. Res.*, *101*, 3957–3972, 1996.
- Plumb, R. A., and M. K. W. Ko, Interrelationships between mixing ratios of long-lived stratospheric constituents, *J. Geophys. Res.*, *97*, 10,145–10,156, 1992.
- Plumb, R. A., D. W. Waugh, and M. P. Chipperfield, The effects of mixing on tracer relationships in the polar vortices, *J. Geophys. Res.*, *105*, 10,047–10,062, 2000.
- Prather, M. J., Numerical advection by conservation of second-order moments, *J. Geophys. Res.*, *91*, 6671–6681, 1986.
- Proffitt, M. H., et al., In situ ozone measurements within the 1987 Antarctic ozone hole from a high-altitude ER-2 aircraft, *J. Geophys. Res.*, *94*, 16,547–16,555, 1989.
- Rex, M., et al., Subsidence, mixing, and denitrification of Arctic polar air measured during POLARIS, *J. Geophys. Res.*, *104*, 26,611–26,623, 1999.
- Salawitch, R. J., et al., Chemical loss of ozone during the Arctic winter of 1999–2000: An analysis based on balloon-borne observations, *J. Geophys. Res.*, *107*(DX), 10.1029/2001JD000620, in press, 2002.
- Schoeberl, M. R., L. C. Sparling, C. H. Jackman, and E. L. Fleming, A Lagrangian view of stratospheric trace gas distributions, *J. Geophys. Res.*, *105*, 1537–1552, 2000.
- Scott, S. G., T. P. Bui, K. R. Chan, and S. W. Bowen, The Meteorological Measurement System on the NASA ER-2 aircraft, *J. Atmos. Oceanic Technol.*, *7*, 525–540, 1990.
- Searle, K. R., M. P. Chipperfield, S. Bekki, and J. A. Pyle, The impact of spatial averaging on calculated ozone loss, I, Model experiments, *J. Geophys. Res.*, *103*, 25,397–25,408, 1998.
- Shine, K. P., The middle atmosphere in the absence of dynamical heat fluxes, *Q. J. R. Meteorol. Soc.*, *113*, 603–633, 1987.
- Sinnhuber, B. M., et al., Large loss of total ozone during the Arctic winter of 1999/2000, *Geophys. Res. Lett.*, *27*, 3473–3476, 2000.
- Sparling, L. C., Statistical perspectives on stratospheric transport, *Rev. Geophys.*, *38*, 417–436, 2000.
- Sparling, L. C., J. A. Kettleborough, P. H. Haynes, M. E. McIntyre, J. E. Rosenfield, M. R. Schoeberl, and P. A. Newman, Diabatic cross-isentropic dispersion in the lower stratosphere, *J. Geophys. Res.*, *102*, 25,817–25,829, 1997.
- Thuburn, J., and D. G. H. Tan, A parameterization of mixdown time for atmospheric chemicals, *J. Geophys. Res.*, *101*, 13,037–13,049, 1997.
- Tuck, A. F., Synoptic and chemical evolution of the Antarctic vortex in late winter and spring, 1987, *J. Geophys. Res.*, *94*, 11,687–11,737, 1989.
- Tuck, A. F., and S. J. Hovde, Fractal behavior of ozone, wind and temperature in the lower stratosphere, *Geophys. Res. Lett.*, *26*, 1271–1274, 1999.
- Volk, C. M., et al., Quantifying transport between the tropical and mid-latitude lower stratosphere, *Science*, *272*, 1763–1768, 1996.
- Waugh, D. A., et al., Mixing of polar vortex air into middle latitudes as revealed by tracer-tracer scatter plots, *J. Geophys. Res.*, *102*, 13,113–13,134, 1997.
- World Meteorological Organization, Scientific Assessment of Ozone Depletion, *Rep. 44*, Geneva, 1999.

J. W. Elkins, D. F. Hurst, and P. A. Romashkin, NOAA Climate Monitoring and Diagnostics Laboratory, 325 Broadway, Boulder, CO 80305-3337, USA. (jelkins@cmdl.noaa.gov; dhurst@cmdl.noaa.gov; promashkin@cmdl.noaa.gov)

A. M. Iwi and W. A. Norton, Atmospheric, Oceanic and Planetary Physics, Department of Physics, Clarendon Laboratory, Parks Road, University of Oxford, Oxford OX1 3PU, UK. (iwi@atm.ox.ac.uk; wan@atm.ox.ac.uk)

O. Morgenstern, Max-Planck-Institut für Meteorologie, Bundesstr. 55, D-20146 Hamburg, Germany. (morgenstern@dkrz.de)

J. A. Pyle, Centre for Atmospheric Science, Chemistry Department, Cambridge University, Lensfield Road, Cambridge CB2 1EW, UK. (john.pyle@atm.ch.cam.ac.uk)

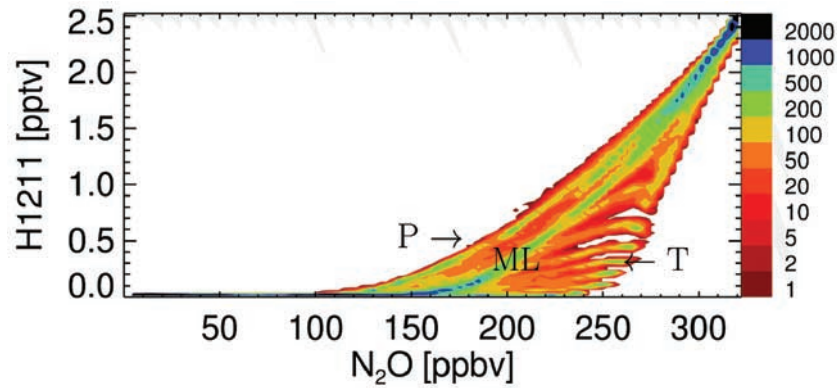


Figure 1. Density plot of halon-1211 versus N_2O for the SLIMCAT integration at 9 March 2000. The model data of the Northern Hemisphere above 342 K of potential temperature are binned into 100×100 intervals of mixing ratio; displayed is the number of grid points per bin. The model comprises 640,000 grid points in the Northern Hemisphere.

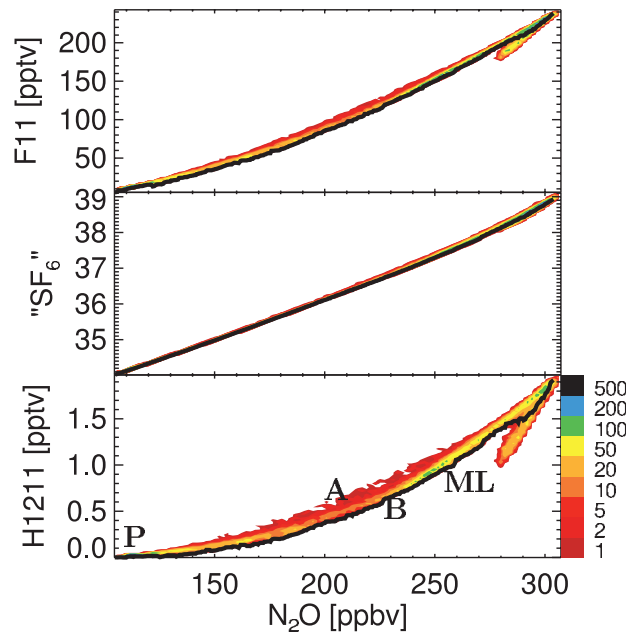


Figure 2. Density scatter plot of CFC-11, SF_6 (arbitrary units), and halon-1211 versus N_2O , for the 451 K isentropic surface at 1 March 2000, 1200 UTC, taken from the SLIMCAT integration. The black lines mark the correlation envelopes $\Psi_i(\zeta; \Theta, t)$.

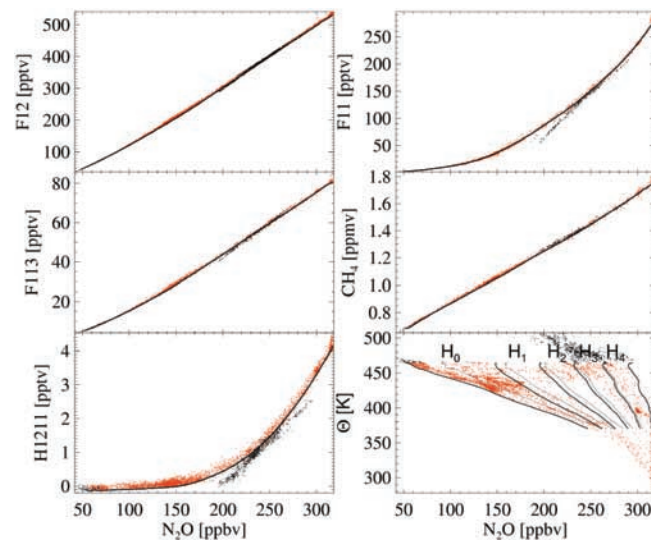


Figure 10. Correlative plots of N_2O versus CFC-12, CFC-11, CFC-113, CH_4 , halon-1211, and Θ , for all ER-2 SOLVE/THESEO 2000 flights. Red dots denote measurements with $\Theta \leq 465$ K, black dots denote those with $\Theta > 465$ K. The black solid lines denote the outer envelopes $\Psi_i(\zeta)$. On the N_2O - Θ plot are superimposed the boundaries ζ_κ corresponding to the “bins” H_0 to H_4 (see text).

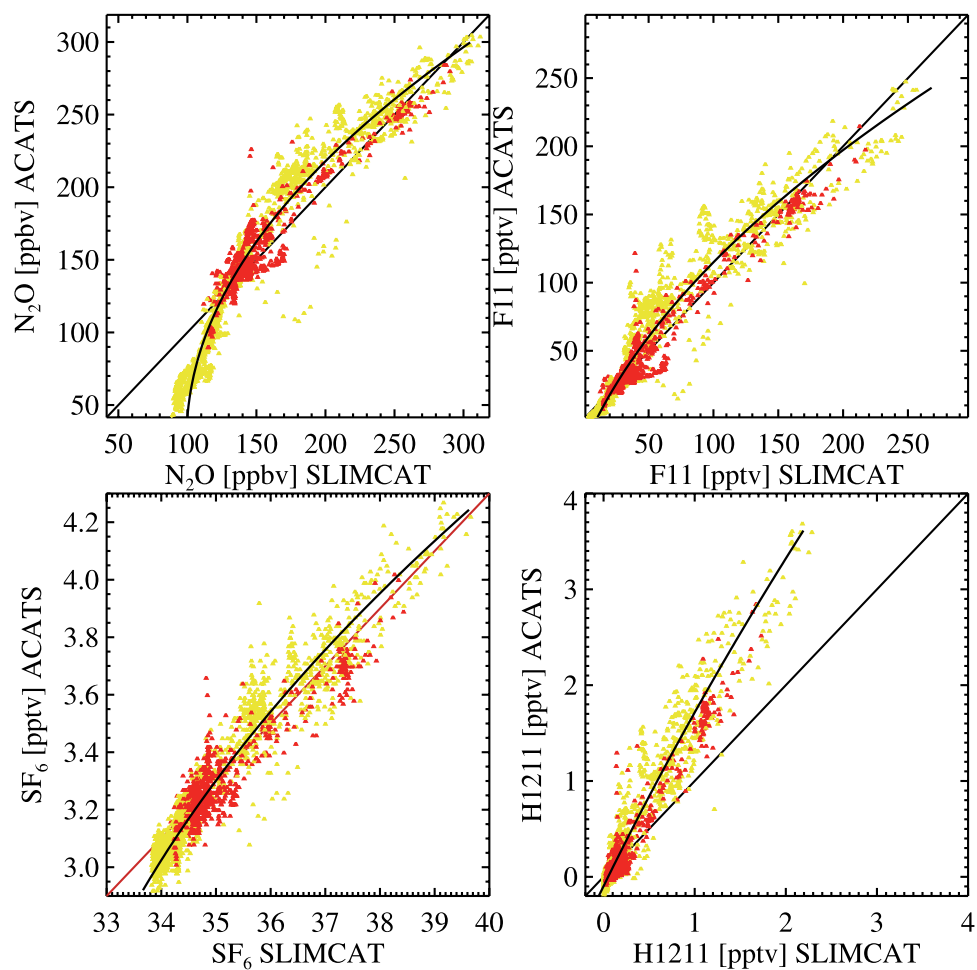


Figure 11. Modeled versus measured mixing ratios for N₂O, CFC-11, halon-1211, and SF₆ (arbitrary units in SLIMCAT). Red symbols depict measurements taken between 9 January and 3 February 2000, yellow symbols depict those between 26 February and 16 March. The solid lines denote the diagonals and the regression parabolas.